COMPARISON OF REYNOLDS AVERAGING NAVIER-STOKES (RANS) TURBULENT MODELS IN PREDICTING WIND PRESSURE ON TALL BUILDINGS

D. Mohotti[1*] and K. Wijesooriya[1], D. Dias-da-Costa[1]
[1]School of Civil Engineering, Faculty of Engineering and IT
The University of Sydney
Darlington NSW 2006
AUSTRALIA
e-mail: damith.mohotti@ sydney.edu.au

Abstract: This paper presents a detailed comparison of using Reynolds Averaging Navier-Stokes (RANS) approach in predicting wind pressure on a super-tall 406 m slender tower with circular cross-section. The results obtained from wind tunnel tests using a rigid model approach in a boundary layer wind tunnel (BLWT) were compared to that of Computational Fluid Dynamics (CFD) numerical simulations. The main objective of this study is to critically investigate the possibility of using RANS turbulent model based CFD approach in tall building design. Three different RANS turbulence models were compared with the wind tunnel data in predicting flow characteristics. The detailed wind tunnel experimental procedure and numerical approach are discussed and presented. It was shown that the shear stress transport (SST) variant model, $k-\omega\ SST$, could predict pressure coefficients comparable to that of the wind tunnel experiments. The influence of flow separation point on flow characterisation and pressure prediction is highlighted. The improvement that can be made in the near-wall region in the finite volume mesh to achieve an accurate separation point is presented. The effects of Reynolds number produced in the wind tunnel and scaled-down numerical models were compared with the anticipated full-scale flow Reynolds number. Hence, it is shown that a correct modelling technique in CFD using RANS turbulence models can be used as an alternative design approach of super-tall structures to estimate wind-induced pressures.

Keywords: Tall buildings; slender structures; dynamic wind, Computational fluid dynamics (CFD), steady RANS

1. INTRODUCTION

The global demand for super-tall structures is increasing, driven by many factors, including the need to provide solutions to highly populated cities, the desire to build iconic landmarks, or even to demonstrate the prowess of a sovereign state. China's Shanghai Tower, Dubai's Burj Khalifa, and the under-construction Jeddah Tower in Saudi Arabia (which is to reach a total height of 1000 m), are a few examples of the recent trend and global competition in the super-tall structures domain. Recent advancements in construction capabilities, materials and design techniques have assisted the ability to build such structures. The design of super-tall structures greater than 300 m in height is usually governed by lateral load stability due to wind loads [1].

Free-standing towers that are used for multifunctional purposes are gaining popularity, especially with advancements in telecommunications technology. Good examples of such structures include Australia's Sydney Tower Eye, Canada's CN Tower, and Malaysia's KL Tower. These structures are slender and generally exhibit circular or rounded sections. Slender structures usually attribute long natural periods of vibration and are sensitive to the dynamic nature of wind. Circular sections advocate a higher frequency of vortex shedding in comparison to commonly used shapes such as squares and rectangles [2]. Concave and curved surfaces generally provide complex flow patterns when air passes around/over them due to their shapes and resulting pressure gradient. Circular and elliptical sections are highly sensitive to Reynolds number, roughness and turbulence [3]. This highlights one of the important aspects of studying the aerodynamic effects of such structures as there is limited research on super tall buildings with circular cross-sections.

The design of tall buildings are included in modern wind engineering codes of practice where approximate procedures for load evaluation and building acceleration are provided. However shape and height limitations are imposed where for the case of a non-typical geometry, experimental procedures in the form of wind tunnel tests are recommended [4]. Also standards such as the AS1170.2:2011 [4] have limitations with regard to the dynamic properties of the building where for structures with

fundamental frequencies of less than 0.2 Hz isn't covered. Since most super tall structures exhibit fairly long natural periods wind tunnel testing is recommended [4].

One of the main outcomes from such analysis is to obtain pressure distributions on the surface of the building using a rigid model approach [1]. In general practice, typical wind tunnel data is used in the design of façades and also can be used for the calculation of lateral loads using a technique known as high frequency pressure integration (HFPI) [1, 5, 6]. However, wind tunnel testing has its own limitations, including the misrepresentation of Reynolds number due to the use of scaled models. The effect of Reynolds number on the pressure coefficients of circular cylinders has been investigated by Roshko [7] and Achenbach [8]. The results showed distinct differences between the pressure values produced by flows with different Reynolds numbers. The values of the Reynolds numbers in full-scale wind flow and the scaled-down models used in a wind tunnel can be significantly different. Practitioners generally employ rough surfaces to simulate turbulent flow which is comparable to real-life conditions; however, this is a rudimentary method as the degree of roughening required to simulate real wind behaviour is unknown. Therefore, substantial parametric studies are required before selecting suitable roughness elements for a given application. In addition, practical constraints such as time, costs and the need for technical expertise can be additional limitations of regular wind tunnel tests.

Computational Fluid Dynamics (CFD) is increasingly used in wind engineering to analyse wind loads, pollutant dispersions, pedestrian-level wind comfort and wind energy harvesting, as discussed by various authors [9-13]. The main advantage of CFD is the ability to simulate full-scale models with the inclusion of full-scale atmospheric boundary layer (ABL) flows within a virtual domain. Also, while parameters are only measured at selected points on the wind tunnel model, CFD provides detailed information about wind velocities, wind pressures, and wind concentration at any grid point within the flow domain [14]. Additionally, in contrast with the conventional wind tunnel methods which require material, labour and time resources, CFD offers more flexibility in conducting parametric studies for different flow conditions, geometries and complex surroundings at a reduced cost [15]. Turbulence modelling is at the heart of CFD, where different models can be employed to simulate the flow of wind. In practical applications of CFD, turbulence models can be broken down into two types, namely, scale

resolving models (large eddy simulations (LES), detached eddy simulation (DES) and scale adaptive simulation (SAS)) and Reynolds Averaging Navier-Stokes (RANS) [16]. LES is a step down from direct numerical simulation (DNS) and unlike RANS, which models all scales of eddies, LES resolves the largest eddies and models the smaller scales by a filtering method based on the computational grid [17]. LES requires a considerable amount of computational power and is usually used as a research tool, whilst RANS is considered in practical engineering applications of CFD. The application of CFD for tall structures has been investigated by various authors where the main subject of these studies has been the 184 m tall CAARC (Commonwealth Advisory Aeronautical Council) standard building, as defined by Melbourne [18]. For instance, Huang et al. [12] showed that CFD results are comparable to that obtained from the wind tunnel. They also investigated the effects of inlet conditions on the mean and RMS (root mean square) pressure variations on the building. Braun and Awruch [19] conducted complex numerical simulations using LES where fluid structure interaction (FSI) for the building was assessed and was found to be comparable to the aeroelastic response obtained from the wind tunnel. Dagnew and Bitsuamlak [20] also employed LES and studied different inflow conditions where pressure measurement readings were studied under these different influences. Zhang et al. [21] performed zonal DES simulation where the unsteady fluid loads are transferred to a structural modal analysis and the resulting building responses were compared to wind tunnel results. More recently, Meng et al. [22] evaluated and compared pressure distributions of a full scale CAARC building in CFD to that of wind tunnel results and showed good correlation. The general consensus from these studies is that CFD can be used in wind engineering applications for tall buildings and show comparable results to that obtained from wind tunnel tests. The CAARC building's popularity is due to its simplistic geometry which offers fairly complex aerodynamic flow. Also, the CAARC building is well-documented as a number of wind tunnel tests have been conducted by several authors and are readily available [18, 23]. Apart from the CAARC building, comparisons of turbulence models on the wind environment around high rise structures [24, 25] and aerodynamic optimisations of building shapes [11, 26, 27] are some other applications of CFD in the tall buildings domain. From these studies it is clear that majority of research on CFD on tall buildings are focused on geometries such as square and rectangular cross-sections. Whilst square and rectangular shapes are considered to be common shapes for low to medium rise buildings, in

the modern world tall buildings usually inhibit curved and rounded surfaces that are aesthetically pleasing. These curved features usually invoke complex aerodynamic flow behaviour around the structure which are different to those observed in square or rectangular cross-sections. The studies mentioned above use high fidelity turbulence models such as LES which show good correlations with experimental outcomes but have achieved this at a high cost of computational time/resources. Also, the ability of certain RANS models such as $k-\omega\ SST$ has scarcely been fully explored for tall buildings. For 2D simulations, $k-\omega\ SST$ has shown to be superior in pressure predictions [28, 29] compared to other $k-\varepsilon$ type models especially for geometries where separation due to adverse pressure gradients is to be expected. Also in more recent application of RANS for structures, Xing et al. [30] showed that the $k-\omega\ SST$ to better predict pressures and capture separation of flow than other RANS models. Hence it is beneficial to explore the capability of current RANS turbulence models on tall structures which exhibit circular cross section or other curved faces in a 3D spatial setting. Existing buildings such as the KL tower in Malaysia and Lotus tower in Sri Lanka are very good examples of such buildings. This calls for a study where a tall building needs to be assessed both experimentally and numerically in CFD beyond the geometry configurations of the CAARC building and other square/rectangular shapes. Most of the available literature investigate buildings with height below 200 m (as highlighted, CAARC building which is 184 m tall) and doesn't qualify as a super-tall structure. Therefore the present study addresses this research gap by presenting comprehensive experimental and numerical investigation on a supper tall building structure with a complex geometry.

As aforementioned, the aerodynamic characteristics of circular cross-sections are quite complex and different to that of square sections. Whilst numerous studies have been conducted for tall buildings with square and rectangular cross-sections, very limited research has been done on circular sections, especially on super-tall structures. Furthermore, there is no clear comparison reported between CFD and wind tunnel data for windward, leeward and crosswind. In this paper, a 406 m super-tall tower with circular cross-sections of varying diameters along its height was studied. A wind tunnel study was conducted in the University of Sydney's boundary layer wind tunnel (BLWT). Numerical simulations in the form of CFD were conducted using ANSYS Fluent [31], and comparisons were made with the

experimental results. The circular cross-sectioned structure was critically analysed, with a focus on providing a practical engineering approach for the wind design of slender super-tall structures. With the increasing trend towards the use of scale-resolved turbulence models, this study aims to achieve accurate prediction of wind-induced pressures by investigating different RANS turbulence models. Furthermore, the impact of scaling is studied in the numerical setting to identify the difference between wind distributions on scaled and full-scale models. Thus, the main aim of this study is to provide an approach which is computationally affordable at obtaining mean wind pressures using RANS as opposed to a more computationally demanding turbulence model such as LES. The study presents various modelling techniques and parameters that users could use to further improve the capabilities of RANS turbulence modelling.

2. EXPERIMENTAL SETUP AND DESIGN

The general geometry of the building was defined by the authors, considering many similar worldwide structures. Mainly inspired by the KL Tower in Malaysia, the tower in consideration is graphically presented in Figure 1, consisting of four key segments, namely the base, shaft, bulb and spire of the tower. The tower is 406 m in height and consists of circular cross-sections of varying diameters. The average diameters at the base, shaft and bulb of the tower are 50 m, 15 m and 24 m, respectively. The height of the tower excluding the spire is 300 m, which means that the spire accounts for approximately 1/4 of the height of the tower. The tower is assumed to be located in a terrain category 2 zone, as defined in AS/NZS 1170.2:2011 [4].

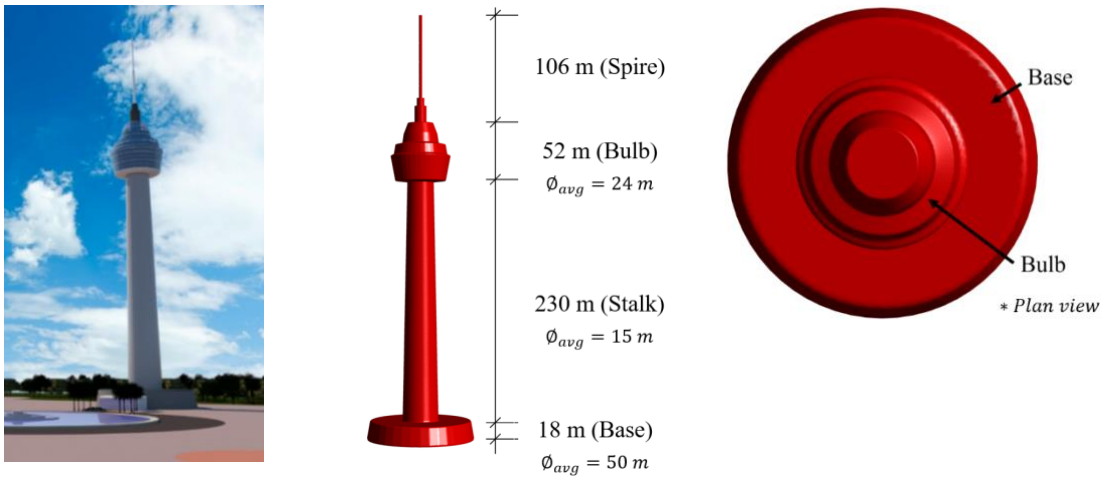

Figure 1: Graphical representation of the tower used in this study

2.1. Model Creation

The foremost step of the modelling procedure involved choosing an appropriate model scale to create an accurate representation of the selected building. Generally, a scale between 1/300th and 1/400th is recommended for buildings [1]. In this study, a scale of 1/300th is used to achieve a satisfactory distribution of pressure points along the height of the building. This also satisfies the blockage ratio requirement from a standard wind tunnel test. The material used in the 3D printing was acrylonitrile butadiene styrene (ABS), which is a flexible (non-brittle) plastic recommended for wind tunnel model preparation. One of the main concerns in the model preparation was the surface finish. The surface roughness of the model can affect the behaviour of flow around circular bodies, which directly affects pressure coefficients on the crosswind face and the leeward face of circular bodies [32]. Hence, a high-quality surface finish was achieved to represent a smooth surface on the model, which is then comparable to the numerical simulation discussed in subsequent sections of this paper. A total of 126 pressure taps were used, with 63 on each side in the windward and crosswind surfaces. The 63 pressure taps were evenly distributed along the height of the building, with an average spacing of 16 mm (5 m in full-scale). Using a large length scale (1:300) enabled a high resolution of pressure taps along the height of the building. The model was printed in parts, as shown in Figure 2, and was assembled together once the pressure taps had been fixed.

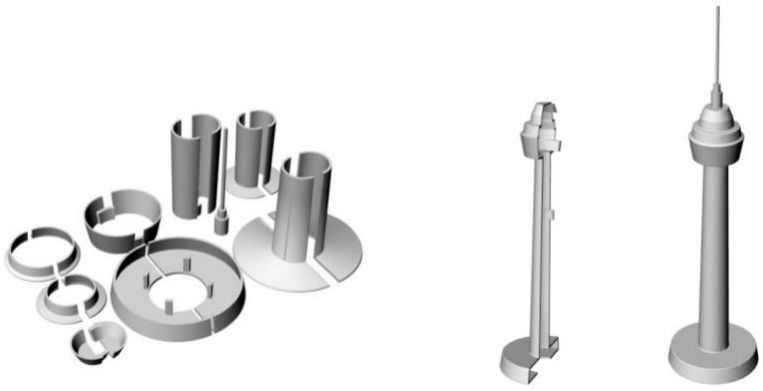

(a) (b) (c)

Figure 2: (a) 3D model parts, (b) half combined, (c) two halves together, once the pressure tube was fixed

2.2. Setup & Preparation

The wind tunnel used for this study was the BLWT in the School of Civil Engineering at The University of Sydney. The tunnel is a closed loop system with a testing section measuring 19 m long, 2.5 m wide and 2 m high. It is capable of handling a top speed of 27 m/s at full capacity. The building was subjected to a turbulent boundary layer flow, where a velocity profile and turbulence intensity profiles were created within the tunnel. The wind profile used for this study was based on AS 1170.2:2011 [4] terrain category 2, with a roughness height (z_o) of 0.02 m. One of the main limitations in using the guidelines of AS 1170.2:2011 for tall and super-tall buildings is the imposed height restriction where profiles are defined up to 200 m. However, the velocity profile can be extended based on the Harris and Deaves model [33, 34]. Similarly, the turbulence intensity profile for terrain category 2 can be extended using Eq. 1 [2], where $I_u(z)$ is the turbulence intensity at any given height z (m).

$$I_u(z) = \frac{1}{ln\left(\frac{z}{z_o}\right)} \quad \text{Eq. 1}$$

The wind and turbulence profiles were generated in the wind tunnel by using roughness elements and spires, as shown in Figure 3. A trial and error process was used, where the blocks were placed in different locations until the appropriate velocity profile and turbulence were achieved at the building location. A cobra probe was used to measure the velocity in three directions at specified increments. Figure 4a shows a comparison of the terrain 2 boundary layer wind profile according to AS 1170.2 and the wind tunnel

tests. The Y-axes are scaled-up to the real height and the X-axes show the normalised velocity at the building location. Similarly, Figure 4b shows the turbulence intensity plot.

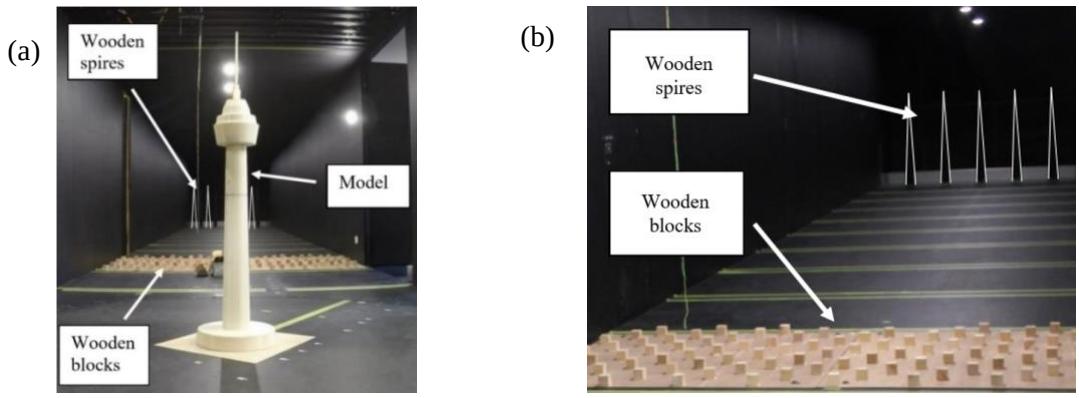

Figure 3: Wind tunnel setup: (a) the building, (b) roughness elements used in the wind tunnel

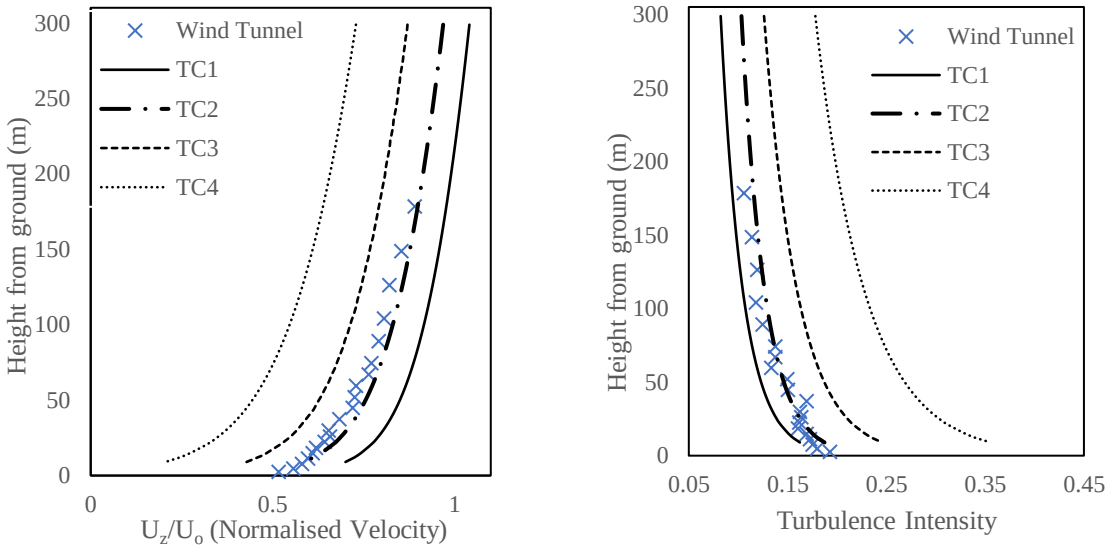

a: Normalised velocity vs height

b: Turbulence intensity vs height

Figure 4: Normalised velocity and turbulence intensity recorded in the wind tunnel and scaled-up to real height

Prior to testing, the wind tunnel was calibrated against atmospheric pressure. The tunnel was also equipped with two pitot static tubes, with one of the pitot tubes fixed to the ceiling. The main purpose of the first pitot tube was to determine the free stream velocity in the tunnel, which was used for setting the tunnel at the correct testing speed. The second pitot tube was located at the reference height of the building, which was approximately 1 m downstream of the building. This was used to record the total and static pressures at the reference height. From this, the dynamic pressure could be determined using Bernoulli's Equation, as shown in Eq. 2. These pressure values, namely the total pressure, static pressure and the dynamic pressure, were then used as normalisation values to determine the pressure coefficients at each pressure tap.

$$P_{static} + P_{dynamic} = P_{total} \quad \text{Eq. 2}$$

The dimensionless pressure coefficients can then be expressed as shown in Eq. 3:

$$C_p = \frac{P - P_{static}}{P_{dynamic}} \quad \text{Eq. 3}$$

where C_p is the pressure coefficient, P is the pressure measured at the tap, and P_{static} and $P_{dynamic}$ are the static and dynamic pressures measured at the reference height by the pitot tube.

Wind tunnel testing in this study was conducted in two phases. The first phase of testing was conducted at a free stream velocity of 12 m/s, where the velocity profile and turbulence intensity profiles were calibrated and matched to that of terrain category 2. The second phase of the wind tunnel tests were conducted with the building model for a duration of 2 minutes per test, with data logged at a frequency of 2000 Hz. This means the pressure readings were logged every 0.5 ms, with a total number of 240,000 pressure readings recorded for each tap. Two minutes at model-scale represent approximately 2 hours in full-scale. Although specific guidelines are not provided, generally the recommended full-scale sampling time is around one hour [35]. The pressure measurements were recorded for each 45° increment, as shown in Figure 5, where A & B mark the locations of the 126 pressure taps (63 each).

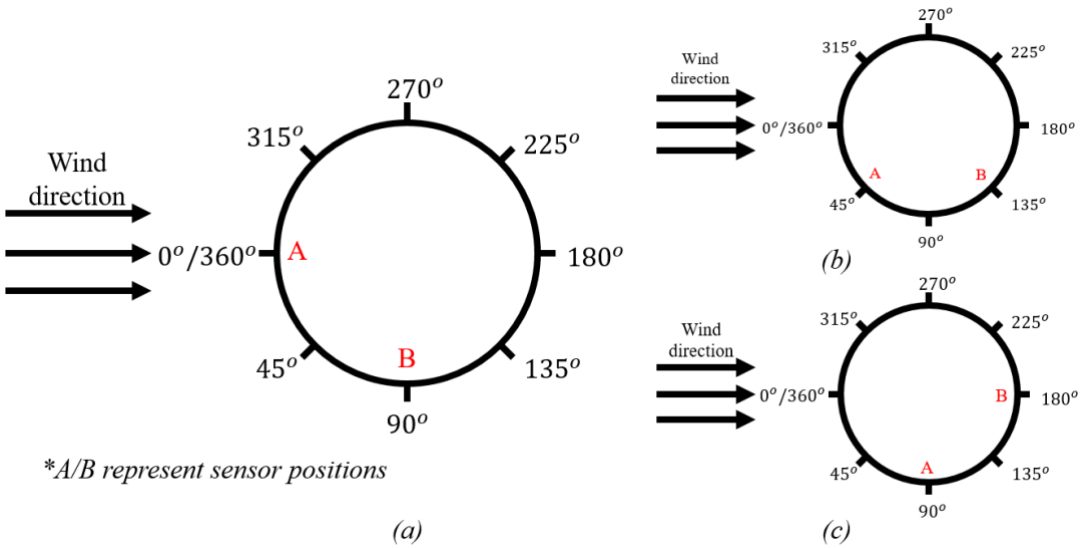

Figure 5 : Test configuration layout where (a) is the start position with sensors "A" facing windward and "B" facing crosswind, (b) model is rotated by 45°, and (c) model is rotated by further 45°

A second set of tests were conducted for a free stream velocity of 12 m/s, where the pressure taps were only active on the windward face. The table was rotated every 20°, and pressure recordings were taken for the same duration and sampling rate as aforementioned. A total of 10 data sets were acquired in

measuring from 0° to 180°. The results from this test were used to compare the pressure distributions around the structure which were captured at a higher resolution as opposed to 45° increments for phase 1. Further validation of the wind tunnel setup is given in terms of the recorded longitudinal velocity spectra. It is understood that wind is dynamic and thus the velocity spectrum is a non-dimensional function describing the change in velocity as a function of turbulence with frequency [2].

The von Karman-Harris mathematical function is commonly used as a comparison in wind engineering. The simulated velocity spectrum used for this study is shown in Figure 6, where it is compared with the von Karman-Harris simulation. Data was recorded at a height of 600 mm from the ground, where an integral length scale of 2.66 m was computed with a mean velocity of 6.2 m/s. The sampling time for this test was 1 minute, with a sampling frequency of 2000 Hz. As can be seen from Figure 6, there is a close correlation between the two curves, which indicates that the wind tunnel setup can be assumed to replicate the turbulence in the atmospheric boundary layer. It is important that the power spectral density recorded in the wind tunnel correlates well with the atmospheric turbulence profile, as it directly influences the peak pressures experienced by the structure [12].

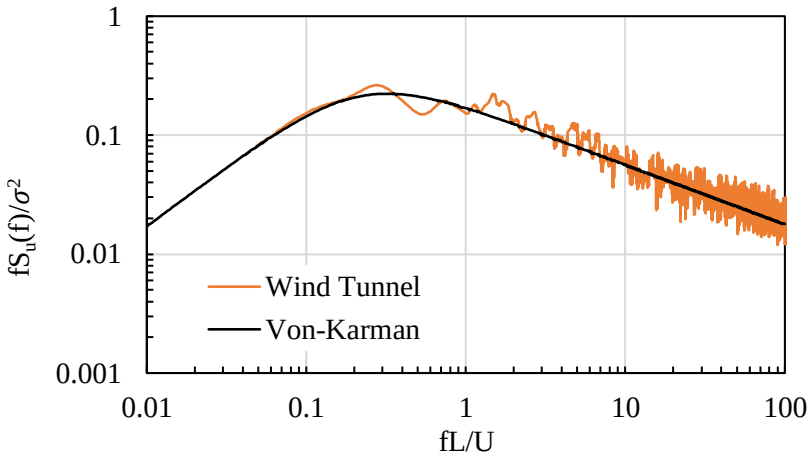

Figure 6: A comparison of the wind tunnel simulated velocity spectrum vs the theoretical von-Karman spectrum

3. NUMERICAL SIMULATION SETUP

3.1. Geometry and Domain Creation

Similar to the experimental setup, a 1:300 scale was adopted in the computational domain where the building was assumed to be rigid. A rectangular enclosure was deemed suitable for the domain, where the size was chosen by performing a parametric study. The domain lengths in the along-wind direction (X-direction), crosswind direction (Z-direction) and height (Y-direction) are 13H, 6H and 3H, respectively, where H is the building height (Figure 7). These limits are reasonably smaller than what has been proposed by Franke et al. [14]. The distance from the building to the outlet was the key parameter in selecting the domain size as this length should be sufficient to capture the wake region behind the building. Furthermore, the recommended blockage ratio, which is the ratio of frontal/projected/cross-section area upon the cross-section area of the test section, should be less than 5% to minimise interaction from the boundaries [36, 37]. The calculated blockage ratio for this particular setup was less than 1%, which is well within the recommended value. Therefore, the domain size used in this study satisfies the conditions required to avoid unnecessary distortion of flow. The interference effect of the domain walls on the flow field around a model is known to be one of the main sources of error affecting the accuracy of numerical data. The boundaries that influence the flow field along the building height are the two sides and the top. Also, the streamlines around the building, which are closer to the wall, are constrained and the flow velocity increases, hence affecting the aerodynamic coefficients. Alteration of streamlines also leads to a change of vortex reattachment and intensity on the leeward side and wake. This is a deviation from the free stream air flow encountered in the natural condition. The symmetry condition with no shear stress applied from the boundary used in CFD replicates values and properties of the air flow, similar to a free stream flow. However, even with such settings, the boundaries need to be at predetermined distances that will not cause artificial acceleration of the surrounding air flow due to its proximity to the building.

The distance between the outlet and the building must also be maintained at a given limit to ensure that it has enough space to create the wake region behind the building. An inadequate space behind the

building can cause non-convergence of the CFD analysis due to the creation of reverse flow. A distance of 10H is provided on the leeward side of the building between the building and the outlet. The space above the building should be large enough to have no influence on flow separation and reattachment at the back end of the building. A height of 3H from the top of the building to the top surface of the domain was provided.

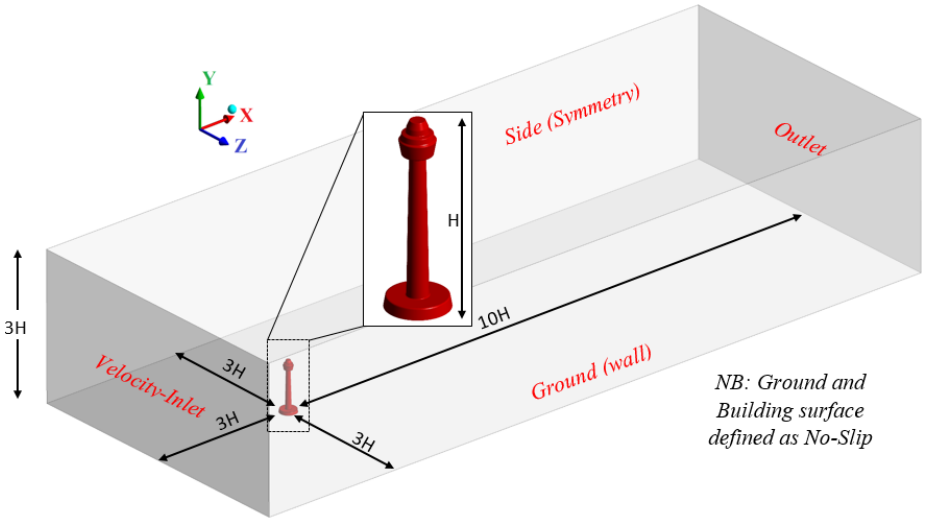

Figure 7: Computational domain size and arrangement of boundaries *(the top and sides are defined as symmetrical boundaries)*

3.2. Mesh Generation

The mesh consists of polyhedral cells, where two refinement zones were given within the volume mesh, including structured face meshing on the surface of the building and an inflation layer, namely zones 2 and 3 (Figure 8a & b). The main purpose of refinement zone 2 (Figure 8a & b) was to ensure that the inlet has an adequate number of cells within the height of the building to generate a sufficient amount of data points which facilitates accurate input and propagation of the velocity profile. Thus, its longitudinal distance was extended from the inlet to the building, and further downstream by an additional 3H. This extended length downstream further enhances the capability to capture the flow behaviour behind the building. The mesh size of refinement zone 3 (Figure 8b) was much finer than zone 2 and located closer to the building. It was defined as a circular cylinder larger than the base diameter of the building. A fine refinement region close to the building can capture the necessary complex flow behaviour around it. Zone 1 was described as the global volume mesh zone, where larger

sizing for the grid was defined at regions further away from the building location. A lower resolution of cells can be employed here as these volume cells are redundant in order to capture the flow and instead serves to maintain continuity within the domain.

The surface mesh of the building is shown in Figure 8c and the inflation layers defined at the surface are shown in Figure 8d. The number of inflation layers and the first cell height are two important parameters that help in capturing the viscous sub-layer flows at the wall boundary. A simple steady RANS (SRANS) model can be used to measure the y^+ at the surface of the building. Figure 9 shows a scatter plot of the y^+ measured on the surface of the building on its along-wind and crosswind directions. Both Franke et al. [14] and Tominaga et al. [37] recommend the use of prismatic cells in the inflation layers. However, the required number of layers, growth rate, and first cell height are problem-specific. For this study, twenty layers of inflation were given at a growth rate of 1.15, which was sufficient to capture the boundary layer flow on the surface of the building. Furthermore, a y^+ of less than 1 ($y^+ < 1$) was required to accurately determine the separation point of the flow at the wall of the building.

Five separate mesh configurations were studied for grid independency, consisting of very coarse, coarse, medium, fine and very fine mesh configurations (named as M1, M2, M3, M4, M5 (Figure 10)). Table 1 contains the properties of the five different mesh types. The accuracy of the results produced by the five mesh regimes are presented in Section 4.1 where a comparison is conducted between them.

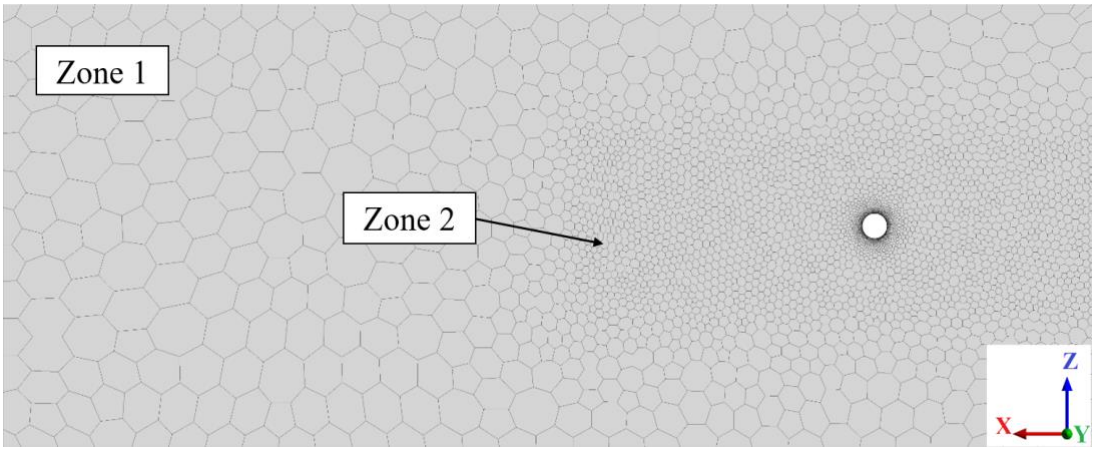

(a)

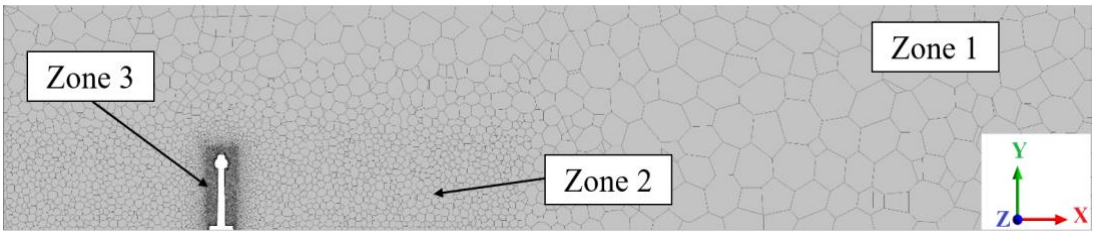

(b)

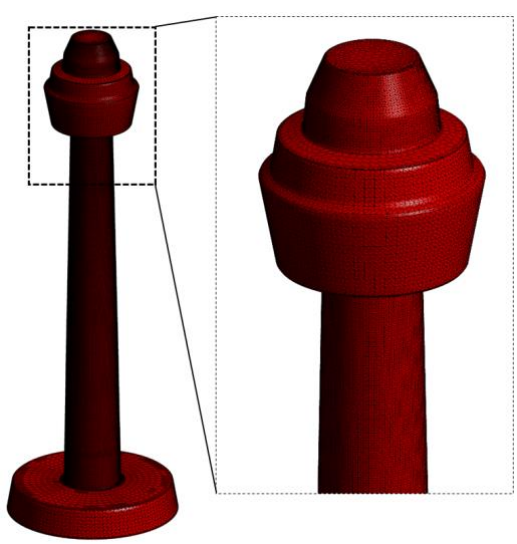

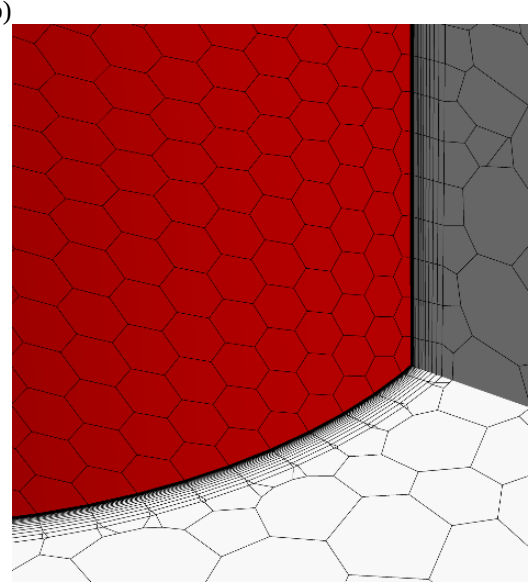

(c) (d)

Figure 8: Polyhedral mesh for the numerical simulation (a) shows the top view of the ground mesh, (b) shows the side elevation view of the mesh cut at a plane $z = 0$, (c) close-up view of the building and mesh, (d) close-up of building surface mesh and depiction of inflation layers on the building

295

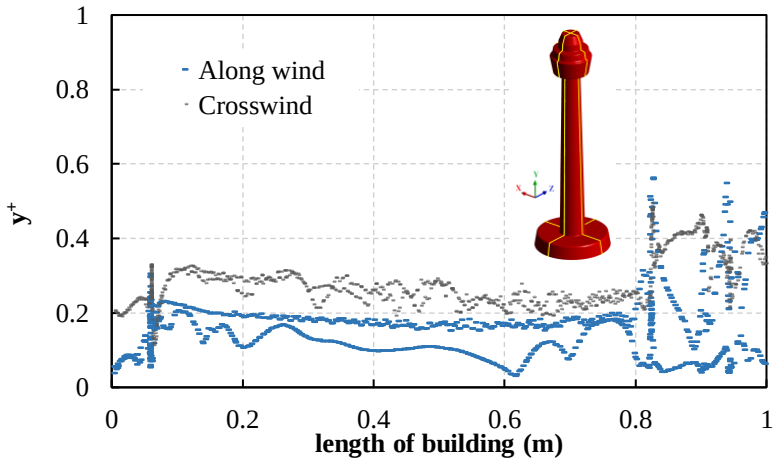

Figure 9: y^+ on the building surface on the along-wind and crosswind directions

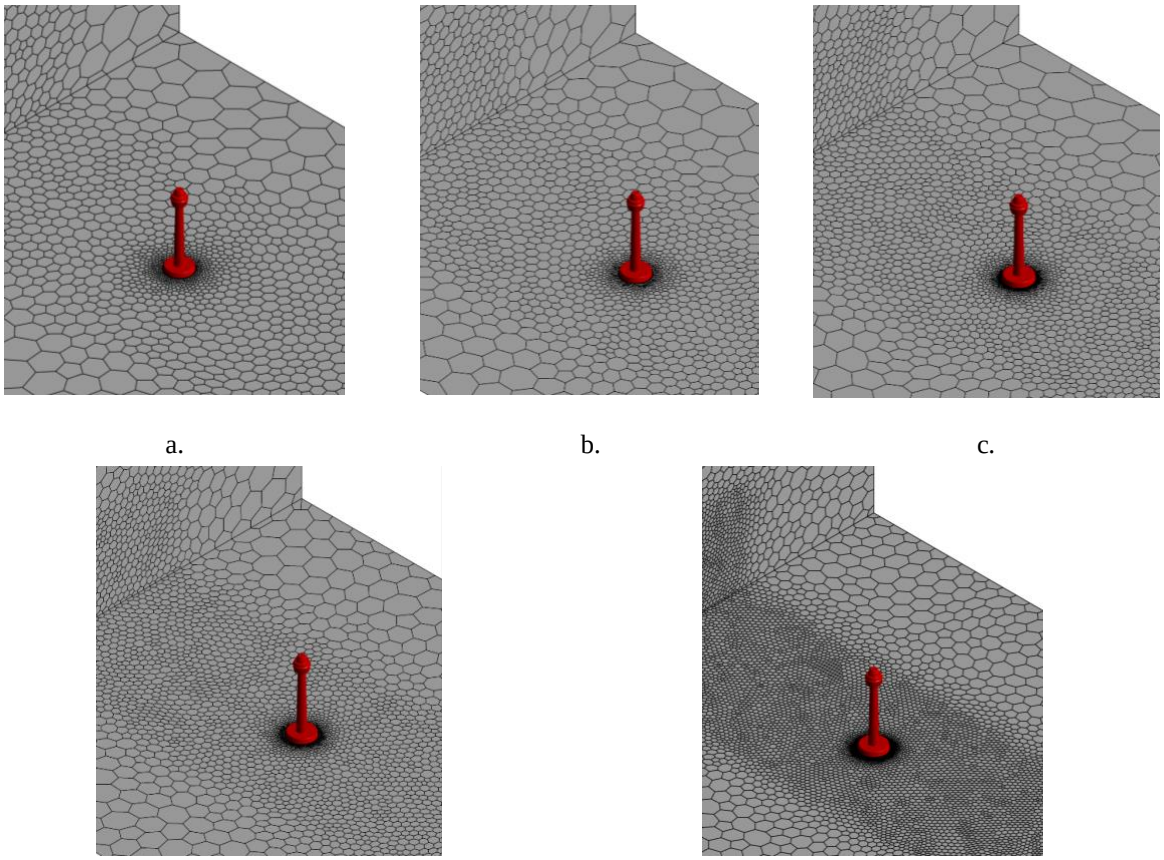

a. b. c.

d. e.

Figure 10: Close-up view of mesh regimes on the ground surface and inlet for: (a) M1, (b) M2, (c) M3, (d) M4, (e) M5

Table 1: Mesh regime properties

Properties	**M1**	**M2**	**M3**	**M4**	**M5**
Zone 1, Volume mesh size (m)	0.5	0.5	0.4	0.3	0.2
Zone 2 size (m)	0.15	0.125	0.1	0.085	0.06
Zone 3 size (m)	0.02	0.0125	0.01	0.0085	0.006
Inflation layers	10	20	20	20	20
Building surface mesh divisions	40	40	60	70	80
Total elements	0.6 m	1.2 m	1.9 m	2.4 m	3.0 m

3.3. Turbulence Modelling and Settings

There are six turbulence models available in ANSYS Fluent that are each suited to different applications depending on the nature of the problem. They are mainly categorised into Reynolds- Average-Navier-Strokes (RANS) models, direct numerical simulation (DNS) and large eddy simulation (LES). Using RANS models, statistically steady solutions of flow variables are determined by averaging the equations over time and over all turbulent scales. DNS involves using very fine computational grid elements to directly solve the Navier-Stokes equations to predict relatively accurate turbulent flows. In the LES

method, Navier-Stokes equations are spatially filtered such that only the large-scale flow variables are directly solved, while smaller eddies are not directly predicted. In this study, where a computational time-efficient method was a focus, RANS models are considered as they are relatively easy to employ and generally provide credible results within a reasonable timeframe. Time efficiency is a concern in regular design office problems, therefore a two-equation RANS model is mostly preferred where time averaging simulations (SRANS) are employed. The most prominently used RANS model is a two-equation standard $k-\varepsilon$ (SKE) model [38], which is always the starting point of many computational wind engineering (CWE) problems.

In this study, three different turbulence models were compared, namely the realisable $k-\varepsilon$ (RKE) model developed by Shih et al. [39], the $k-\omega$ turbulence model developed by Wilcox [40] and its shear stress transport (SST) variant, $k-\omega$ SST [41]. Finally, the four-equation transition SST model developed by Menter et al. and Langtry et al. [42, 43] was used. This model is computationally demanding when compared to the two-equation models. The differences of mesh resolution near the wall are displayed in Figure 11, where the different near-wall mesh treatments for $k-\varepsilon$ models and $k-\omega$ models could be found from the left to the right, and y_P is the distance from the wall to the adjacent layer. The dimensionless wall distance y^+, as defined in Eq. 4, was introduced to evaluate the grid resolution near the wall:

$$y^+ = \frac{u_\tau y_P}{\nu} \qquad \text{Eq. 4}$$

where u_τ is the friction velocity based on wall shear stress and air density, and ν is the kinematic viscosity.

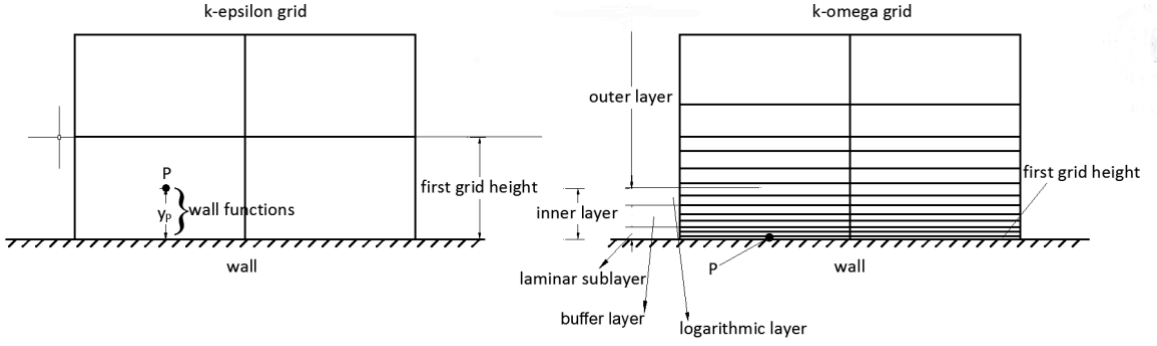

Figure 11: Schematic representation of near-wall mesh for k-ε and k-ω models

The $k-\varepsilon$ realisable model was employed with three different wall function settings. First, the standard wall function (SWF) approach was employed where the default mesh was modified in order for the y^+ value to be in the range of 30 to 100. This change was made because it is known that in ANSYS Fluent the boundary layer is broken down into two layers, an inner layer and an outer layer, as shown in Figure 11. The inner layer is composed of three parts, a laminar layer, a buffer layer and a logarithmic layer. The laminar sub-layer and buffer layer are defined as having a $y^* < 11.225$, and the log region is defined by $y^* > 11.225$ where the standard wall functions are active and work best when $30 < y^+ < 300$ [44]. y^* is an alternative definition of the dimensionless wall distance and is defined in Eq. 5,

$$y^* = \frac{u_\tau^* y_P}{\nu} \qquad \text{Eq. 5}$$

where u_τ^* is the friction velocity based on the turbulent kinetic energy k_P in the wall-adjacent cell centre point P and on the constant C_μ which is taken as 0.09 [44].

Resolving the laminar sub-layer flow is essential to accurately depict the point of flow separation at the surface of the body. Hence, the use of wall functions may not be suitable for flows concerning circular cylinders. It is understood that wall functions are employed for cases where separation of flow is not to be expected and to save computational effort by providing a relatively large inflation layer at the face of the wall. For most industrial flows and novice users of CFD, a combination of a $k-\varepsilon$ turbulent model coupled with standard wall functions is employed.

Secondly, a $k-\varepsilon$ realisable model with standard wall functions option was used where $y^+ < 1$. At such a low y^+, the laminar stress relationship is employed in ANSYS Fluent where $y^* = U^*$ is active at the boundary layer, thus overruling the use of wall functions [44].

Finally, a second $k-\varepsilon$ realisable model is employed with the default mesh where $y^+ < 1$, but using the enhanced wall treatment option in ANSYS Fluent. The enhanced wall treatment combines the two-layer model with enhanced wall functions with the help of a blending function in order to smoothly transition from resolving the laminar sub-layer to the turbulent region based on a calculated turbulent Reynolds number [44]. A second-order upwind scheme was used for the spatial discretisation of the turbulent kinetic energy and momentum, and turbulent dissipation rate transport equations. Also,

second-order discretisation was used for pressure. The algorithm used for the pressure-velocity coupling was the Semi-Implicit Method for Pressure-Linked Equations - Consistent (SIMPLEC).

Solution convergence is one of the most important criteria that needs to be addressed in CFD simulations. Convergence of the solution plays a major role in the final result of the simulation in fact the low convergence criteria can inhibit the accuracy of the final result.

Both Franke et al. and Tominaga [14, 37] have stated that a default CFD code convergence limit of 0.001 is lenient in order to achieve a converged solution. Blocken [36] acknowledged the default 0.001 convergence criteria to be inadequate and recommended that steady state simulations have to be carried out until the scaled residuals taper out to have a zero gradient. In this study, a different approach was adopted to determine if the solution has converged by meeting the following criteria: (1) monitor drag coefficient of the building where the simulation is run until no significant change in the value is observed over iterations; (2) residual scales to taper to a constant value, adhering to Blocken's recommendation as stated above; (3) convergence of scaled residuals of X, Y, Z momentum to 10^{-6}, continuity 10^{-6} and k, ω & ε to 10^{-5}.

For steady state simulations, one assumes the solution is to be steady after a number of iterations. Monitoring of drag coefficient till it achieves a constant value was the method adopted to determine the convergence of the solution. It was found that a steady value for the drag coefficient was reached when the scaled residuals reached a constant steady value. The limits of convergence criteria mentioned above in point (3) were imposed after it was observed that there were many simulations where criteria 1 and 2 were satisfied but the scaled residuals were below these limits. These stated limits were also implemented into the simulation such that a definitive end can be achieved without user interference.

It must be noted that the imposed limits of the scaled residuals (limits for momentum, continuity and k, ω & ε) are problem-specific and factors such as domain size, grid size and blockage ratio all contribute in achieving convergence [14, 36, 37].

3.4. Inlet and Boundary Conditions

Comparisons between wind tunnel testing and CFD can only be made if the same experimental conditions are replicated within the computational domain. Inflow boundary condition is the most important as it defines the wind velocity and the turbulence profiles at the inlet, which need to match with those implemented in the wind tunnel experiments. The inflow velocity, $U(z)$, is defined as a logarithmic profile as shown in Eq. 6:

$$U(z) = \frac{u_\tau}{\kappa_{ke}} \ln\left(\frac{z + z_o}{z_o}\right) \quad \text{Eq. 6}$$

where u_τ is the friction velocity, z_o is the roughness height measured in the experimental scale, and κ_{ke} is the von Karman constant which is assumed to be 0.42 for all applications of the $k - \varepsilon$ model. The turbulence at the inlet was defined by calculating the kinetic energy as given in Eq. 7 [37]

$$k(z) = a(\bar{U}(z) I_u(z))^2 \quad \text{Eq. 7}$$

where $\bar{U}(z)$ is the mean speed, $I_u(z)$ is the turbulence measured from the experiment, and "a" takes a value of 1.5 as isotropic turbulence is assumed. The turbulence dissipation rate and specific dissipation rate is as given in Eq. 8 and Eq. 9, where C_μ is a model constant and is taken as 0.09 [45, 46].

$$\varepsilon = \frac{u_\tau^3}{\kappa_{ke} z} \quad \text{Eq. 8}$$

$$\omega = \frac{\varepsilon}{k C_\mu} \quad \text{Eq. 9}$$

Also, a surface roughness at the ground is given on the basis of the relationship of sand grain height (k_s) and roughness length relationship. It is as given in Eq. 10 [47], where c_s is known as the roughness constant and takes a value between 0.5 and 1. The provided surface roughness and the resulting calculated sand grain height ensures that the first cell height is larger than this value, as required in ANSYS Fluent [44].

$$k_s = \frac{9.793 z_o}{c_s} \quad \text{Eq. 10}$$

A change in velocity profile and turbulence intensity is to be expected downstream, and the difference in change can be ignored if they are relatively small at the building location [47]. A series of preliminary simulations was carried out in an empty domain consisting of the same mesh arrangement as that defined

as M3. The profiles were obtained at the building location and compared with the wind tunnel and AS 1170.2 predictions. Figure 12 shows a comparison between the experimental velocity profile, the input velocity profile measured at the inlet, the velocity profile downstream at the building location and the extrapolated terrain category 2 profile. Figure 12a shows the velocity profile comparisons, where the X and Y axes measure normalised velocity and height (with regard to a reference height of 1 m), respectively.

As can be seen, the difference between the profiles measured at the building location are minimal, where only some minor discrepancies were observed at the bottom of the structure, which can be ignored, especially in the analysis of super-tall buildings. Also, Figure 12b shows the turbulence intensity profile where the X and Y axes measure turbulence intensity against the normalised height (at reference). The comparison between the turbulence intensity of terrain category 2 from AS 1170.2 and that used in the inlet show good correlation between them. The surface roughness plays an important role in the propagation of the inlet conditions. Whilst roughness is achieved by the placement of blocks in the wind tunnel (trial and error), for CFD a surface roughness needs to be defined as mentioned before. In this study, much like the wind tunnel, the roughness height (z_o) was initially estimated to be 7×10^{-5} (derived from scaling down real roughness height 0.02 m for terrain category 2) and roughness constant, $c_s = 1$. Trial and error procedure within the empty wind domain was used for fine adjustment of roughness parameter especially in matching the turbulence intensity profile at the target building location.

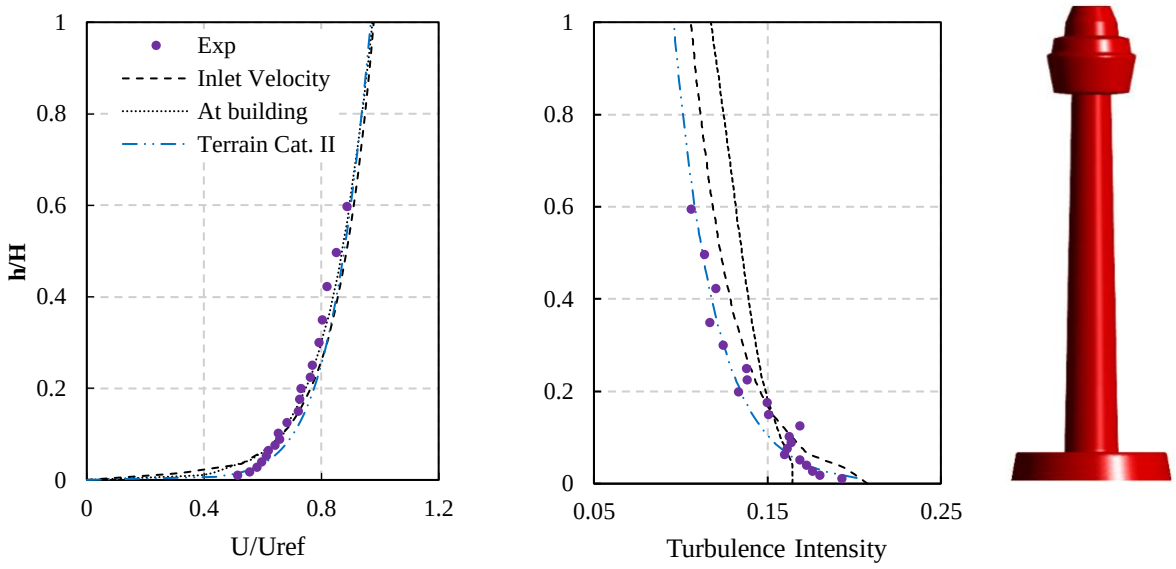

(a) Velocity profile (b) Turbulence intensity profile

Figure 12: A comparison of profiles measured numerically (inlet and building location), in the wind tunnel and AS/NZS 1170.2:2011

As a summary, the boundary conditions were defined as follows: (a) ground surface defined as rough-no slip wall, (b) the inlet with the abovementioned boundary profiles, (c) the sides and top are defined as symmetry conditions, (d) the outlet as a pressure outlet with zero gauge pressure and the building surface defined as a no slip wall.

4. RESULTS AND DISCUSSIONS

4.1. Grid Sensitivity Analysis

A grid sensitivity analysis was performed in order to obtain an optimal grid size using the SRANS $k-\omega\ SST$ turbulence model. This eliminated discretisation errors in providing a coarse mesh, and also reduced the computational time in providing an undesirable finer mesh. Five mesh sizes were studied and the mesh properties are given in Section 3.2. The pressure coefficient (C_{pe}) variation along the height of the building for the different mesh arrangements are displayed in Figure 13 for windward, leeward and crosswind faces. As observed from Figure 13a, for all mesh configurations the windward pressures are almost identical with minor differences. However at leeward (Figure 13b) and crosswind (Figure 13c) faces the discrepancy of the very coarse mesh, M1, is apparent. In comparison to the other configurations, the leeward pressure for M1 is over predicted and for the crosswind face under predicted

at regions 0.4 h/H to 0.8 h/H. To further elaborate the above point, Figure 14 shows the absolute deviation from the experimental values for the five different mesh schemes where windward, leeward, crosswind and average is shown. As it can be seen there is a notable improvement from the transition of M1 to M2 with regard to solution discrepancy. However from M2 to M5 the percentage reduction of the deviation is not significant. The difference observed in results between the M2, M3, M4 and M5 mesh configurations are insignificant. Similar observations were reported in studies conducted by Meng et al. [22] and Elshaer et al. [48] where hexahedral and polyhedral cells were used respectively. From this study and the other two studies cited previously, it can be concluded that once an optimal mesh configuration has been achieved, further refinement of the mesh has diminishing returns with regard to pressure prediction accuracy and incidentally affected the simulation time. Based on these observations, mesh scheme M3 was selected as the preferred mesh configuration for this study. M3 was used for the rest of the models discussed in this paper as it offers a balance between accuracy and computational time. A notable difference between the five mesh configurations and the wind tunnel results was observed in the leeward face. This will be discussed in detail in subsequent sections of this paper.

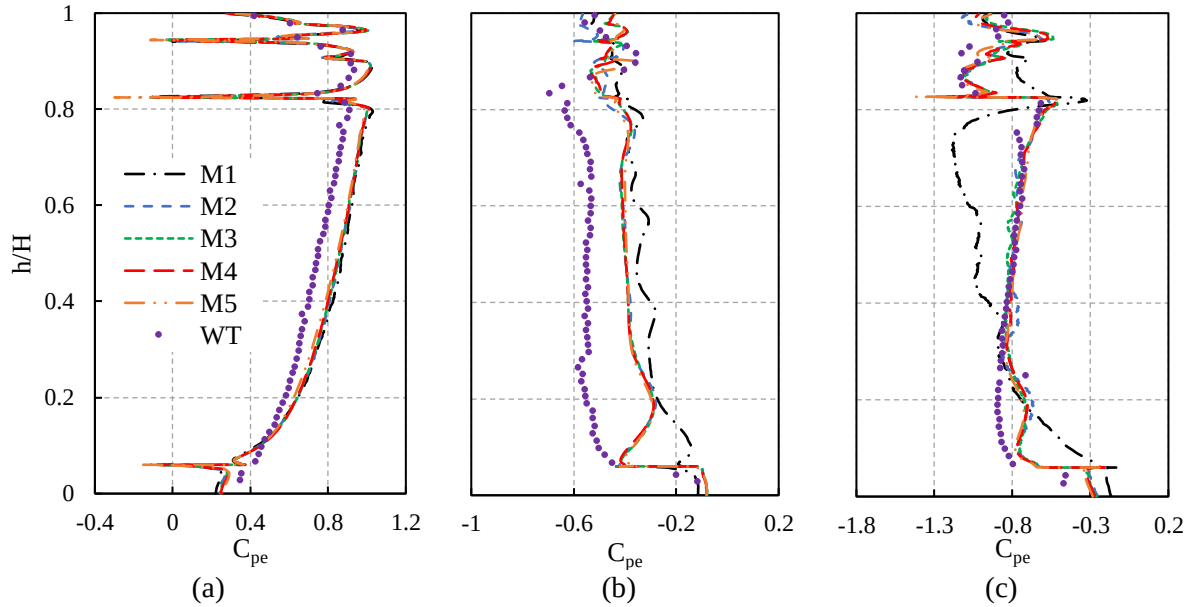

Figure 13: Results for mesh study comparisons (a) at the windward face, (b) at the leeward face, and (c) at the crosswind face

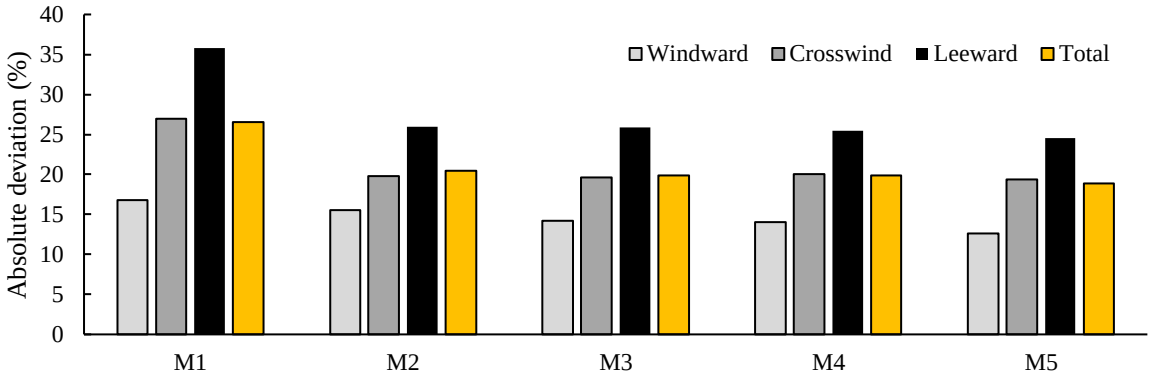

Figure 14: Absolute deviation for windward, crosswind, leeward and total pressure

4.2. Influence of the Turbulence Model

4.2.1. Windward, Leeward and Crosswind Pressures

As mentioned in Section 3.3, the three turbulence models selected for this study were: realisable $k-\varepsilon$, $k-\omega\ SST$ and the four-equation transition SST. The realisable $k-\varepsilon$ model was tested for three different wall functions. Practical applications of CFD are still constrained to RANS turbulence modeling. Hence, these models were selected due to their ability to model flow within a reasonable time frame. The performance of three different turbulence models were compared with the wind tunnel test results based on the pressure coefficients obtained on the surface of the building. It must be noted that all turbulence models were run on the default M3 mesh with the exception of the $k-\varepsilon$ with standard wall function case where y^+ was modified. Table 2 shows the abbreviated terms used for the different test cases used for the turbulence modelling comparison and in the discussions to follow.

Table 2: Classification of turbulence models

Turbulence Model	$k-\omega\ SST$	$Transition\ SST$	$k-\varepsilon\ Realisable$ (SWF $y^+>30$)	$k-\varepsilon\ Realisable$ (SWF $y^+<1$)	$k-\varepsilon\ Realisable$ (EWT)
Abbreviation	TM1	TM2	TM3	TM4	TM5

Figure 15a to c show the variation of C_{pe} along the height of the building for windward, leeward and crosswind faces, respectively. The CFD results are compared with the experimental values obtained

from the boundary layer wind tunnel tests (referred to as "WT") where a free stream velocity of 12 m/s is considered.

Figure 15a displays the results on the windward face of the building and shows that all model types over-predict pressure coefficients. It must be noted that the over-prediction of the C_{pe} in TM3, TM4 and TM5 is higher than that in TM1 and TM2. However, the general pattern of variation is consistent in comparison to the wind tunnel flow results where the prediction of TM1 and TM2 fall closest to that of wind tunnel results.

For the leeward face (Figure 15b), the difference between the experimental and computational values are quite large when compared to the windward face. All models capture the pressure distribution pattern over the height of the building well where the TM1 model is the closest to the experimental values, closely followed by TM2. The deviation of results for the $k-\varepsilon$ type model from the wind tunnel results, especially in the case where TM3 is observed. TM3 has large deviations, by almost three times, in comparison to the experimental values. This is because the use of standard wall functions, with $y^+ > 30$, has rendered the flow to be fully turbulent thus ignoring the viscous sublayer flow. Furthermore the computation of eddy viscosity for realizable $k-\varepsilon$ are different to that of the $k-\omega\ SST$. The $k-\omega\ SST$ model not only includes a damping coefficient to transition to low-Reynolds number formulation but also account for the transport of turbulence shear stress [41, 44]. This improves its ability to predict flows where adverse pressure gradients are to be expected [41]. The difference between TM4 and TM5 are relatively small along the height of the building, with TM4 predicting slightly closer pressure values than TM5.

At the crosswind face (Figure 15c), TM1 showed the closest pressure predictions to those of the experimental values. The results for TM1 show almost identical behaviour and predictions both from the values and trends of the C_{pe} variation. The variation of the TM2 model is comparable to the experimental values, albeit under-predicting pressures at the shaft of the building. TM3 and TM5 severely under-predict pressure values, with the former showing the largest deviation. However, the TM4 model seems to give the closest prediction among the $k-\varepsilon$ type models with predictions of both C_{pe} variation and values along the height of the building.

The wind pressure contours for the tower is displayed in Figure 16. At the windward surface (Figure 16a) it is clear that the maximum pressure occurs at the bulb of the structure which is roughly at a height of 0.85 H. Further along the height of the structure, maximum pressure region diminishes to zero and shifts to negative pressures as the wind detaches at the apex. Also the pressure on the windward face slowly decreases on its sides as observed from the contour bands and transitions to negative values at the crosswind face (Figure 16c). Large suction pressures, especially at the bulb, are observed that are higher than the windward pressures where absolute values are considered. The accelerating fluid around the structure causes the positive pressure to transition to negative suction pressures as the flow passes from windward to crosswind face. This is clearly visible by the contour bands in both Figure 16a & c. A peak negative pressure is observed at the crosswind face where it diminishes as the flow reaches the leeward face. These observations are consistent with previous work by Roshko and Achenbach [7, 8] for circular cylinders. At the leeward face the pressures are negative due to the flows inability to fully recover and are as observed Figure 16b. It can be seen that the bulb of the building accumulates the largest pressures and is the most critical where local pressures are concerned.

The following sections will delve deeply into causations of the pressure discrepancies observed for the different turbulence models used in this study.

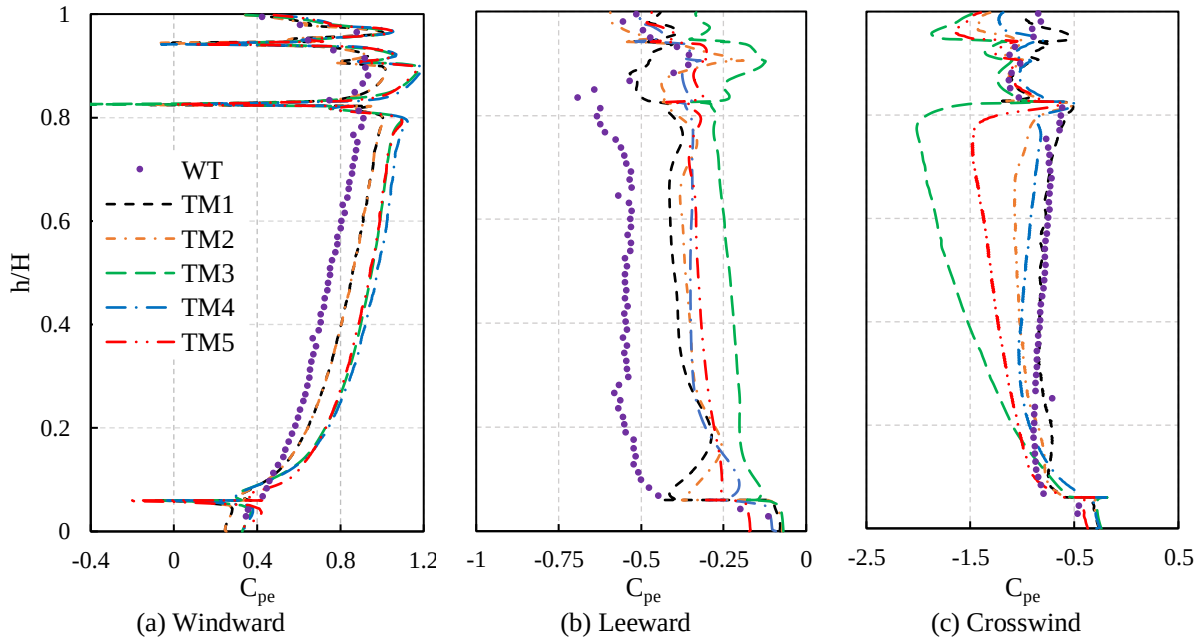

(a) Windward (b) Leeward (c) Crosswind

Figure 15: Pressure distribution comparisons for different turbulence models

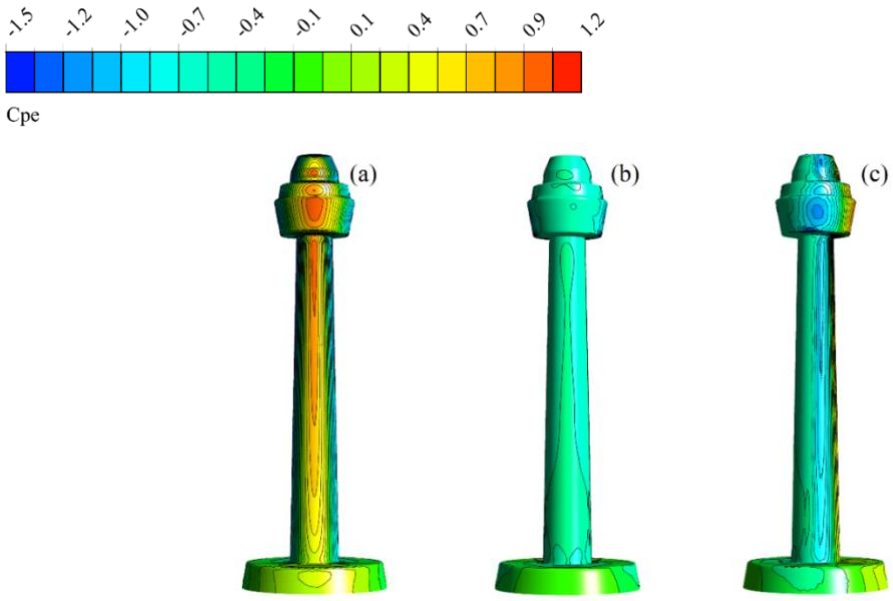

Figure 16: Mean C_{pe} distribution for TM1 model, (a) Windward face, (b) Leeward face (c) Crosswind face

4.2.2.Flow Separation Point

Where circular cross-sections are concerned, surface pressure measurements are highly reliant on the surface boundary flow. The point of separation of the flow needs to be accurately determined in order to correctly predict pressures on the surfaces of a building. Unlike square cylinders, circular cylinders do not have sharp edges which advocate the separation of flow around the body. Flow separation that occurs on a circular cylinder is due to the combination of the fluid's viscous forces, shape, and the adverse pressure gradient experienced. The boundary layer flow or momentum of the fluid is reduced to zero, which then creates a reverse flow at the surface of the body. The location at which this boundary layer flow reaches zero is the point of flow separation. Figure 17 shows the flow streamline for the five different turbulent model configurations at the same cross-sectional height of the tower (700 mm from the ground). They show a clear depiction of the arch vortex created behind the structure as wind flows past them. There is a distinguishable difference when models, TM3 (Figure 17c) and TM5 (Figure 17e), are compared to the other models with regard to the size of the vortex formed. It is clear for TM3 and TM5, separation of the fluid doesn't take place until the fluid has reached further downstream past the crosswind face which results in the smaller vortices formed. This also results in a larger negative pressure at the crosswind face and recovery pressure (less negative) at the leeward face. This observation

coincides well with the outcomes shown in Figure 15c where it can be seen that TM3 over predicts largest negative pressure on the crosswind face followed by TM5. Also TM3 is the largest at under predicting negative pressures on the leeward face followed by TM5. The differences of models TM1, TM2 and TM4 cannot be observed from the streamline plots alone.

Accurate depiction of the location at which point of separation takes place is not clear from observing the arch vortex formations alone. The wall shear stress plot around the circular cylinder can give a better indication. Wall shear stress (τ_ω) is defined as the shear stress in the fluid close to the boundary wall of flow where the layer of fluid is within the boundary layer. It is calculated as given in Eq. 11, where μ is the viscosity of the fluid, U is the flow velocity parallel to the wall, and y is the perpendicular distance from the wall.

$$\tau_\omega = \mu \frac{\partial U}{\partial y} \qquad \text{Eq. 11}$$

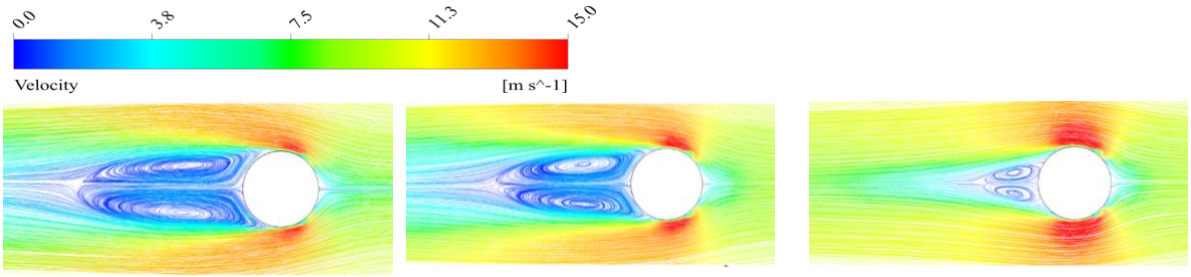

(a) k-ω SST (TM1) (b) SST transition (TM2) (c) k-ε $y^+ > 30$ SWF (TM3)

(d) k-ε $y^+ < 1$ (TM4) (e) k-ε EWT (TM5)

Figure 17: Velocity streamlines around the circular cross-section of the building at a height of 700 mm from the ground (located in the shaft)

Figure 18 shows the variation of wall shear stress around the cross-section of the building at the height of 700 mm from the ground for wind angles varying from 0^o to 180^o. The wall shear stress starts at zero (at the windward face, 0^o), which then rises to a peak and then drops to cut the x-axis where the shear stress becomes negative. The location at which this transition from a positive to negative shear stress is observed, is the point at which flow separation occurs.

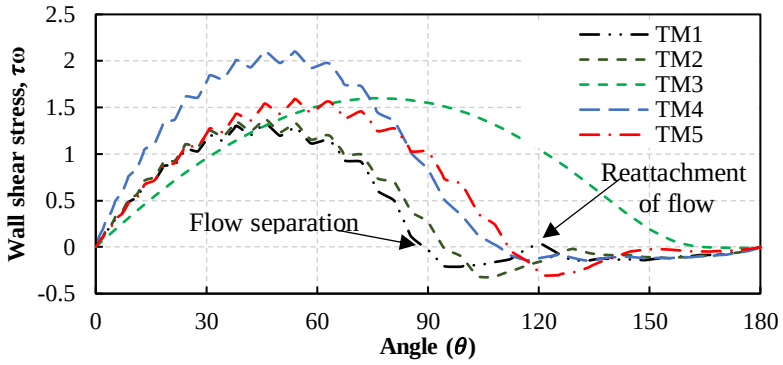

Figure 18: Plot of wall shear stress around the face of the building at 700 mm from the ground

From Figure 18, it is clear that TM1 has the earliest point of flow separation that occurs before the crosswind face (90°), followed by TM2, TM4, TM5, and lastly TM3. The stark differences between the SST models and the $k-\varepsilon$ type models are clear where the former undergoes flow separation at a location further upstream in comparison to the latter. Whilst the effect of this is not directly correlated with the crosswind pressure, there is an observable trend with the leeward pressures observed. The recovery of pressure at the leeward face diminishes with an earlier point of separation. This means that the earlier the separation, the lesser the recovery of pressure expected at the leeward face of the structure.

4.2.3.Flow Field Investigation

Figure 19 shows the contour plots of windward direction streamlines on a vertical plane cut through the centre of the building. It is observed for TM1 the existence of three clear circulation zones (at the top of the bulb, at the bottom of the bulb and at the base) in the wake of the structure. The circulation zones that occur at the wake, near the top, is due to the flow separation that occurs as flow passes over the bulb. This can be verified if the streamlines are carefully observed, where at the windward face of the bulb, the trajectory of the flow streams point upwards which indicates the fluid masses flowing over the building. The separation accelerates the fluid, which reduces the pressures (as observed in Figure 15) in accordance to Bernoulli's principle, and creates vortices in the wake due to the reattachment of the flow stream. As observed from Figure 19c, the wake recirculation of flow is relatively small for the realisable $k-\varepsilon$ (TM3) model in comparison to the others. Furthermore, the resolution of the wake recirculation formed is also poorly captured by the TM3 model. The small size of the wake circulation formed for

TM3 indicate less negative pressures which was observed in section 4.2.1 where leeward pressures were concerned. This is followed by TM5 (Figure 19e) where the circulation of flow is larger than TM3 but is marginally smaller than TM1, TM2 and TM4 (Figure 19a, b and d).

The SST models (TM1 and TM2) displays better detail of recirculation regions, in comparison to the $k-\varepsilon$ type models, where the SST models captures three recirculation zones, as mentioned afore. The $k-\varepsilon$ models vaguely represent one recirculation zone, with the one at the base being omitted. The importance of these features are accentuated when observing pressures at sensitive locations such as the bulb of the structure where many geometry changes are present.

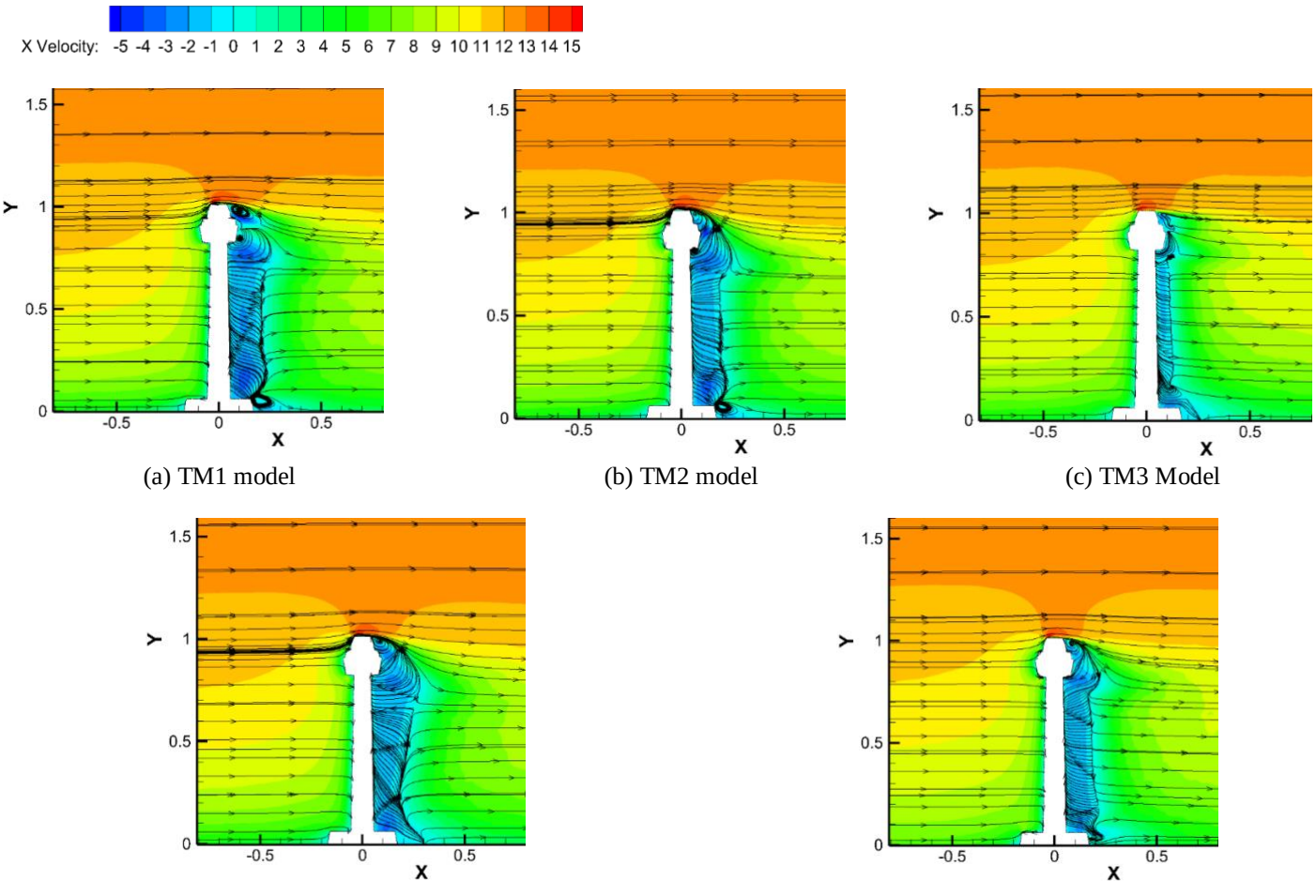

(a) TM1 model (b) TM2 model (c) TM3 Model

(d) TM4 model (e) TM5 model

Figure 19: Contour plots of X-velocity and streamline plots at X-Y plane, Z=0

4.2.4. Turbulent Kinetic Energy

Over-prediction of windward pressure by the $k-\varepsilon$ type model is evident in all three variations used. The difference between two types of RANS models can be visualised in Figure 20 where a comparison for TM1 and TM4 is shown (for brevity) in terms of contour plots, showing the surrounding turbulent kinetic energy for a side elevation of the building. The kinetic energy at the vicinity of the windward face of TM4 is high compared to TM1. This increase in kinetic energy of the prevailing wind results in the over prediction of windward pressures for the $k-\varepsilon$ type models. Similar development has been observed by other researchers and are compatible with the observation of this study [12, 49]. Thus, the over-prediction of windward pressures with the use of a $k-\varepsilon$ type model was expected, even with the improved realisability constraints applied in the development of the realisable $k-\varepsilon$ model [39]. The $k-\omega\ SST$ (TM1) model also over-predicts the windward pressure, but as mentioned before, the deviation is roughly within 10% of the experimental values which is deemed to be within reasonable limits.

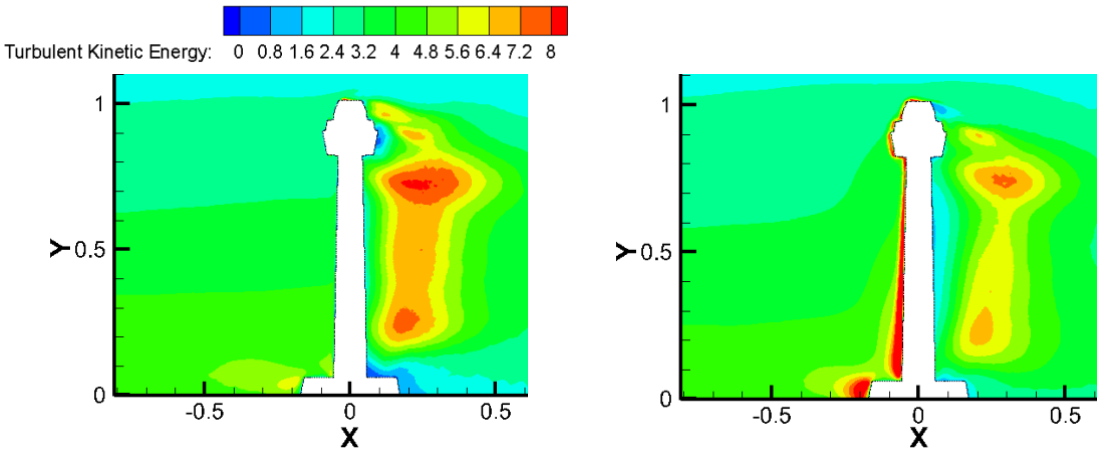

(a) TM1 (b) TM4

Figure 20: Kinetic energy contour plot from side elevation of the building

4.2.5. Section Discussion and Improvements

The consensus from this series of tests is that the $k-\omega\ SST$ model gives the best result of the turbulence models employed. Much of this is attributed towards the ability of modelling the flow all the way up to the wall where the boundary layer flow is concerned. Such stringent first cell height and mesh parameters are required, especially due to the low Reynolds numbers considered for these tests. The

leeward pressure distribution also showed improvement with the use of the $k-\omega\ SST$ model. However, the deviations between the experimental and CFD results for the leeward pressure is still significant. To quantify the difference between the experimental (WT) and numerical (CFD) $k-\omega\ SST$ the Pearson correlation coefficient (R) can be applied. A linear relationship between the two data sets should be observed if they were to exactly match each other. Table 3 displays the correlation coefficients for all three faces and as it can be observed both windward and crosswind pressure show strong correlation, 0.94 and 0,84 respectively. The leeward face however show a lower correlation of 0.47 in comparison to the other two faces. Figure 21 displays the scatter plots for C_{pe} values for the experimental and CFD simulation where a linear regression line is fitted. For the windward face (Figure 21a) a correlation (R^2) of 0.88 was calculated. A high correlation of this order was expected where windward pressures were concerned. For the crosswind face (Figure 21c), a moderately high correlation of 0.66 was observed. However, the leeward face (Figure 21b) observed low correlation of 0.22 which indicates that a significant difference between the experimental and numerical such that only 22% of the variance is related to the fitted regression line.

From the above analysis the difference between experimental and numerical results on the leeward pressure is evident. One of its main contributing cause is the used of steady state flow as this ignores the unsteady inflow turbulence of the incoming flow. For bluff bodies, the pressure on the leeward face is effected due to the unsteady wake formations that arise due to vortex shedding. In RANS simulations deficiencies of this phenomenon have been observed [50, 51] which inherently lead to the discrepancy of leeward surface pressure predictions.

Table 3: Correlation coefficient for windward, leeward and crosswind, between experimental and $k-\omega\ SST$

Face	**Correlation Coefficient (R)**	R^2
Windward	0.94	0.88
Leeward	0.47	0.22
Crosswind	0.81	0.66

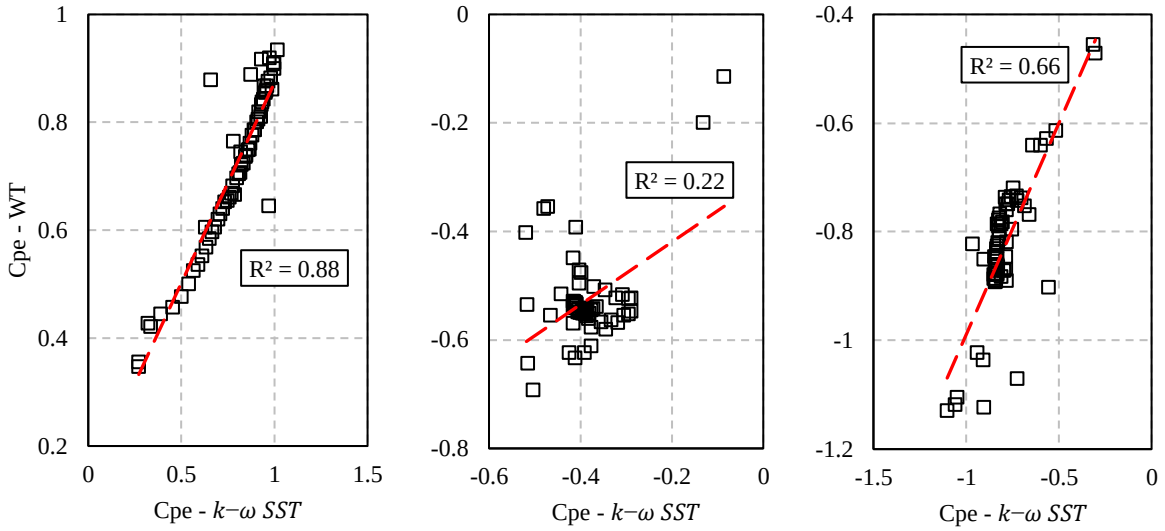

Figure 21: Comparison of $k-\omega\ SST$ (X-axes) and experimental (Y-axes) C_{pe} for: (a) windward face, (b) leeward face and (c) crosswind face

The use of a higher order turbulence model such as that of a scale resolving model can further improve the pressure prediction and capture enhanced flow details that are not observable when using RANS. To demonstrate this, a DDES (Delayed Detached Eddy Simulation) model is used which is a hybrid RANS/LES model such that RANS is employed within the boundary layer and LES in the separated region. There are many variants of the DDES model where different RANS turbulence models could be applied. The $k-\omega\ SST$ DDES model [52, 53] was opted due to the proven capability of the $k-\omega\ SST$ in the windward and crosswind regions as shown in this study. The same mesh configuration was used as that described for M3 including the inlet conditions and the mean pressure coefficients were obtained after sampling for 4 seconds. Figure 22a shows the mean pressure comparison of the leeward side, Figure 22b shows the scatter plots of C_{pe} for the leeward pressure and Figure 22c shows the large scale turbulence structures which are observable in the vicinity of the structure.

As observed from Figure 22a significant improvement in the leeward pressure was observed especially in the region of the base and stalk of the building from heights of 0 to 0.8 h/H. The improvement in leeward pressure prediction is reflected in the R^2 value of 0.454 which is has improved over that which was obtained by RANS $k-\omega\ SST$. The discrepancies located at heights 0.8 h/H to 1 h/H result in the relatively low R^2 prediction when compared to the earlier observed windward and leeward values for R^2. These discrepancies could also be eliminated through careful modelling of the mesh as the requirements for scale resolved models are different to RANS. Also, the vortex structures observed

around the building as shown Figure 22c show important features such as vortex shedding and the horseshoe vortex at the feet of the structure.

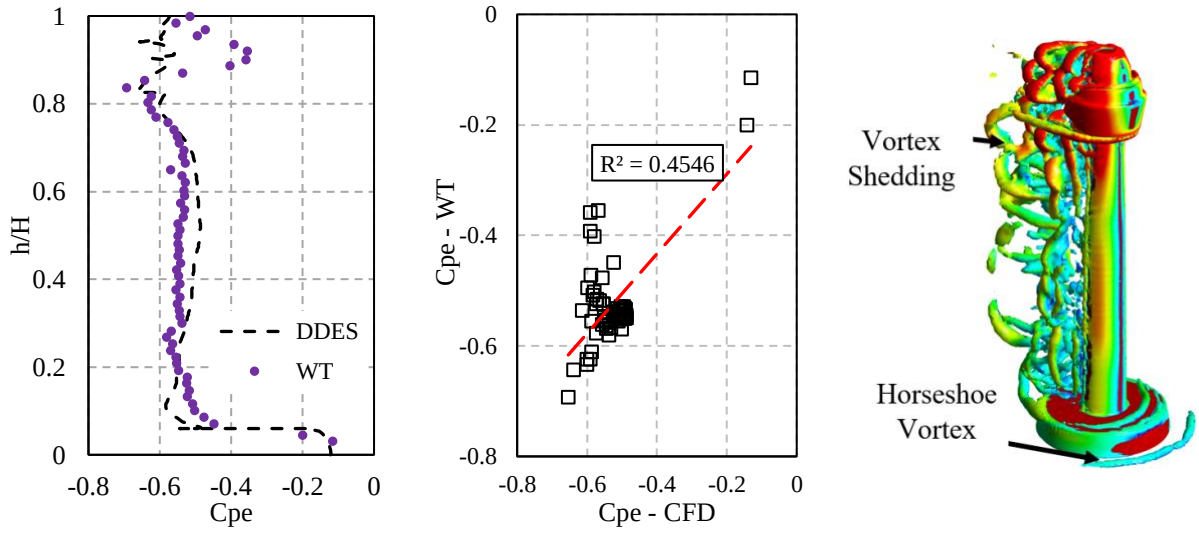

a. Leeward pressure comparison b. Correlation comparison c. Detailed scale structures

Figure 22: Improvement of results from DDES simulation on the leeward face

4.3. Circular Flow Analysis

The pressure distribution around the structure was measured such that the variation was captured at every 20° angle increment. A comparison between the experimental and CFD simulations were performed for the $k-\omega$ *SST* model as it showed better performance in estimating pressure distribution around the structure. The pressure distribution at four different heights were captured and are presented in Figure 23.

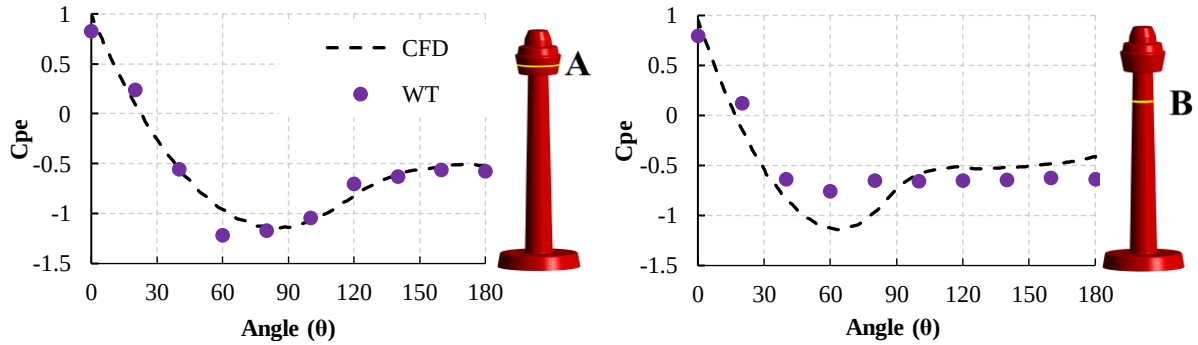

(a) Location A (867 mm from base) (b) Location B (700 mm from base)

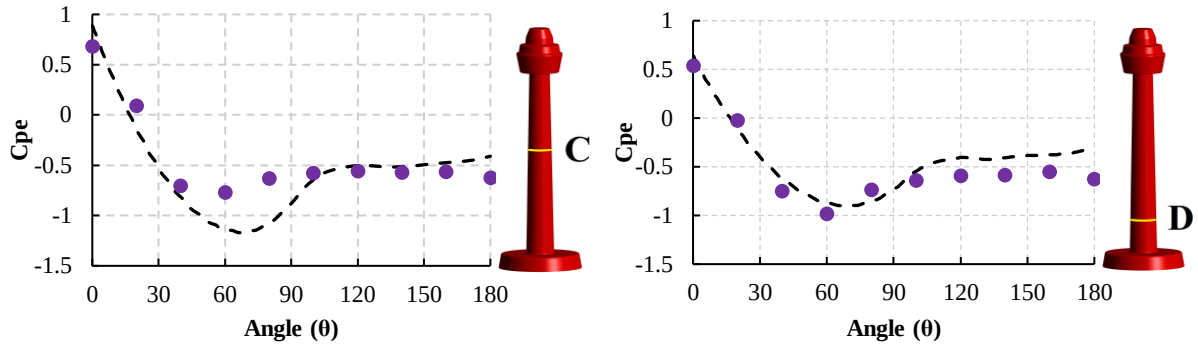

(c) Location C (500 mm from base) (d) Location D (200 mm from base)

Figure 23: The cross-sectional pressure distributions around the structure at locations A, B, C and D

The pressure coefficients measured in CFD are in good correlation with the experimental analysis where both values and distributions are concerned. A notable difference is observed in pressure readings at locations B and C, where the peak negative pressure coefficient is over-predicted by CFD in comparison with the experimental results. This is greatly due to the difference in turbulence level created in the close vicinity of the bulb section by the CFD and experimental studies. Furthermore the measured turbulence intensity at the building location (Figure 12b) is slightly over predicted to that of the experimental. The pressure readings from 110^{o} to 180^{o} for locations B, C and D on the shaft show that the experimental coefficients are higher than the results produced by the numerical simulations. This trend is observed until the leeward face, where differences of below 30% can be calculated, as observed in Section 4.2.1. The outcomes of these pressure distribution results with regard to the differences between numerical and experimental are comparable to the study conducted by Yan and Li on high-rise structures with elliptical cross-sections [54].

The Eurocode 1 [55] is one of the few codes that provide external pressure coefficients for circular cylinders. Hence, it is worth to compare the pressure coefficients obtained from this analysis to that of the Eurocode. Since the pressure coefficients displayed in the Eurocode are for those at the reference height of the building. Locations “A” (at the bulb) and “B” (at the stalk) are compared with Eurocode 1 as they are the closest to the reference point, which in this case is the apex of the structure, and are as shown in Figure 24.

Observing Figure 24a and b it can be seen that the pressure coefficient distribution at the bulb differs greatly from the Eurocode prediction for a Reynolds number of 5×10^5. The peak negative pressure is approximately 50% of that predicted in the Eurocode 1. It can be summerised that a clear difference between the pressure coefficient distribution between the Eurocode and the current study has been observed.

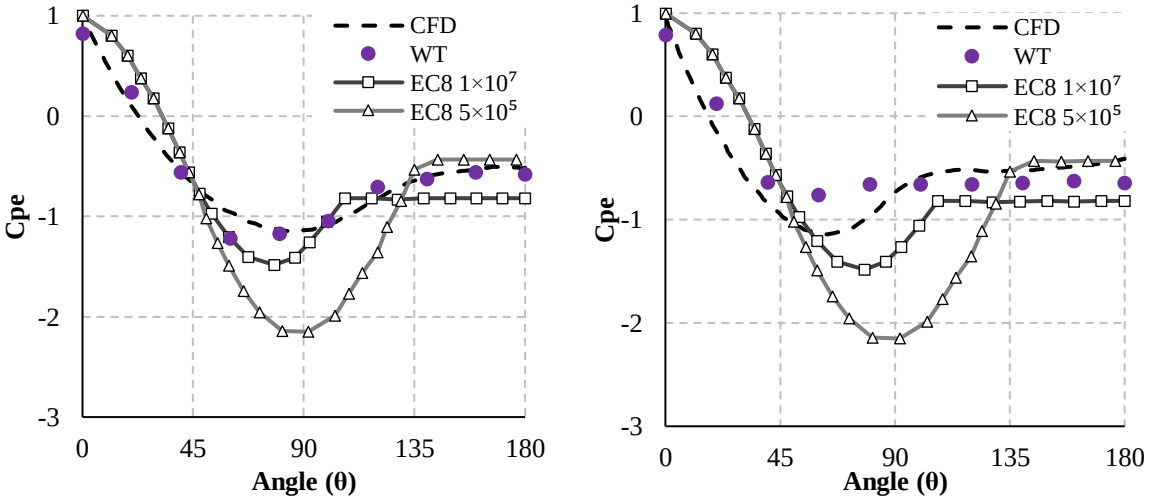

(a) Location A, at bulb (b) Location B, at stalk

Figure 24: Pressure coefficient comparison between experimental, numerical and Eurocode 1.

4.4. Reynolds Number Effect

The flow of wind around structures with circular cross-sections is drastically affected by the Reynolds number, as mentioned earlier in this paper. The study conducted by Achenbach [8] for a circular cylinder showcases the differences in flow states with changing Reynolds numbers. The cross-sectional dimensions of the building used in this study varies along the height of the building. The average Reynolds number calculated for the given structure for a free stream velocity of 12 m/s is 2×10^5.

The analysis performed in this section examines the difference between flow behaviour and pressure distribution observed on the structure, between that of the scaled-down and the full-scale models. The scaled-down model used the dimensions of the wind tunnel (TM1), while the other model was developed with the actual dimensions of the building (RS2). The full-scale structure would attribute a total height of 300 m, where it was subjected to a wind flow with a free stream velocity of 50 m/s. In the model RS1, the fluid properties were altered such that the Reynolds number matches the wind tunnel and the scaled-down CFD model. RS2 used unaltered fluid properties where high turbulent wind flow was experienced.

Table 4 summarises the evaluation performed where the calculated Reynolds number is based on the diameter at the shaft of a building at the non-dimensional height of 0.7.

Table 4: Model comparisons for full-scale test series

Model	Wind velocity	Viscosity of air	Reynolds Number
RS1	50 m/s	$0.02\ (kg/ms)$	8×10^4
RS2	50 m/s	$1.7894 \times 10^{-5}\ (kg/ms)$	1×10^8

Figure 25 shows a comparison of the pressure distributions for the windward, crosswind and leeward sides, where direct comparison of RS1 and RS2 is made with TM1 and the wind tunnel test. A good correlation between RS1 and TM1 can be observed in all three directions, where the difference between them is no more than 5%. This shows that by altering the Reynolds number of the full-scale building, one could simulate the wind tunnel scale behaviour. RS2 shows the pressure distribution for the building at its full-scale, where fluid properties are not constrained. As can be observed from Figure 25a, the pressure variation at the windward faces does not show a significant variation. However, the leeward and the crosswind faces experience a noticeable variation in pressure between the scaled-down and full-scale models. This is attributed towards the variations in the Reynolds number experienced by the structure at its full-scale in comparison to the scale-down models. The kinetic energy of the wind flowing past the structure is considerably higher for the case of RS2. This is due to the acceleration of wind around the structure causing a large suction force as per Bernoulli's principle. This is verified when Figure 26 is observed where the graphical representation of pressure distributions of the full-scale model in comparison to TM1. It is noticeable how the negative pressures developed on the side are significantly higher in regions between the windward (0^o) and the crosswind (90^o) faces. With large negative pressure distributions located within this region, the resolved forces act in the opposite direction to that of the along-wind force. This means that the overall drag force on the structure is over-predicted if one were to use the scaled down pressure coefficients. Also, the local pressures on the façade could be severely under predicted which could lead to instability of both nonstructural and structural members at these locations.

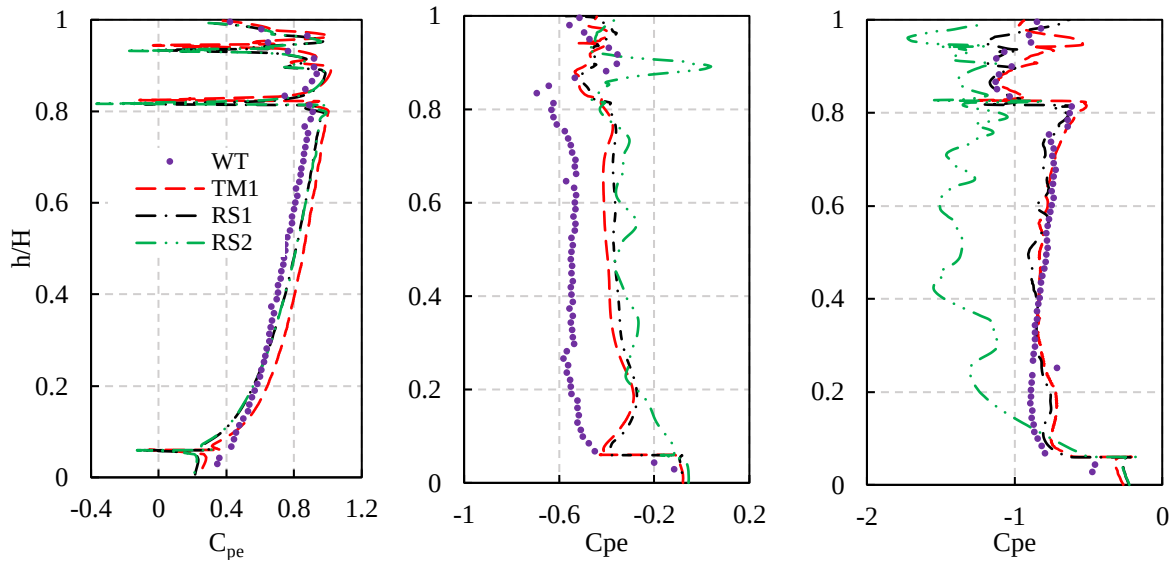

Figure 25: Pressure distribution comparison between WT, TM1, RS1 and RS2

687

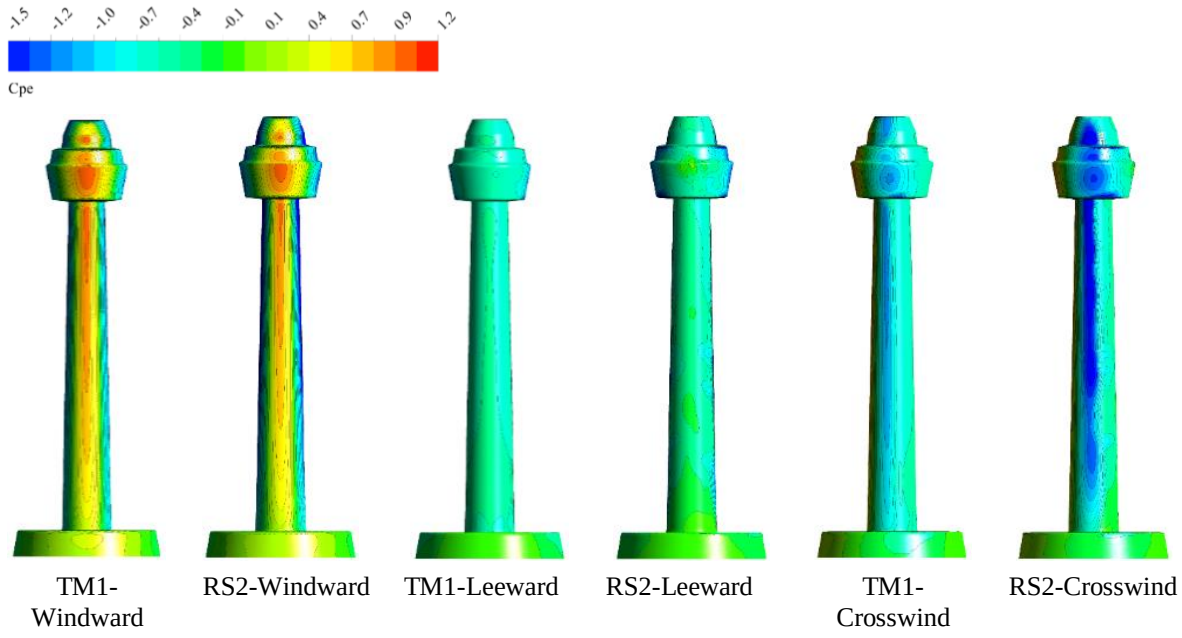

Figure 26: Graphical representation of pressure distribution for TM1 and RS2

688 **5. CONCLUSIONS**

689 This paper presented a comparative study performed on mean wind pressure obtained from
690 computational fluid dynamics (CFD) and wind tunnel approaches for a slender super-tall structure of
691 406 m. The main focus of the study was to investigate the ability in using of RANS models in prediction
692 of wind induce pressure on tall buildings. Three different types of turbulence models were employed

693 which included the two-equation realisable $k-\varepsilon$, $k-\omega\ SST$, and transition SST models. Different
694 wall functions were investigated for the $k-\varepsilon$ model, as it is deemed as the industry standard where
695 open flows are concerned. The influence of Reynolds number on the pressure reading was investigated
696 for Reynolds numbers ranging from 10^4 (model scale) to 10^8 (full-scale). Thus, from the present study,
697 the following conclusions can be drawn upon;

698 • From the three different turbulence models used in this study, the $k-\omega\ SST$ model showed
699 the closest prediction of pressure coefficients of the structure when compared with the wind
700 tunnel results performed at the same Reynolds number.

701 • It was shown that identification of the flow separation point is essential in achieving the correct
702 flow characteristic in CFD analysis. The results revealed that to achieve this, a dimensionless
703 wall distance (y^+) of less than 1 was required.

704 • Streamline plots show that the vortices formed behind the structure directly correlates to the
705 point of flow separation which determines its size. The differences between the turbulence
706 models and its ability to correctly predict flow separation is evident when observing these plots.

707 • A comparison of pressure distribution for a circular body with the Eurocode 1 was made. It was
708 shown that the pressure predictions by using Eurocode 1 is conservative at low Reynolds
709 numbers. It also showed that the magnitude of pressure and its distribution pattern were
710 significantly different from each other when compared to both numerical and experimental
711 results. Thus leading to the conclusion that the code shouldn't be used for the estimation of
712 pressure of super tall structures.

713 • In the case for a full scale model it was shown that CFD results were closely matched with the
714 wind tunnel data when its Reynolds number was matched to that of the wind tunnel scale. When
715 the CFD analysis was performed at full-scale, the results showed disparity from the wind tunnel
716 results. The full-scale model with its unaltered Reynolds number flow of 1×10^8, showed to
717 have differences in terms of pressure predictions where the side suction is concerned. It was
718 clear that the overall dynamic drag had reduced due to this, and significant differences were
719 observable between the model-scale and the full-scale.

As a summary, use of CFD in predicting wind pressure on super-tall buildings can be considered as an alternative option to wind tunnel testing. It was shown that the accurate selection of turbulence models, wall functions, mesh configuration and model-scale improve the accuracy of the results generated from CFD analysis. One of the limitations of this study is the use of a steady solver and the resulting assumption of a smooth inflow. This limits the output to a time averaged solution where instantaneous pressure fluctuations cannot be monitored. Therefore, the method used in this study can be recommended for a preliminary design stage of a tall building where approximation of pressure values are sufficient. In order to further improve prediction of mean pressures, especially on the leeward face, the use of higher fidelity turbulence models such DDES model can improve predictions as shown. Also these transient simulations will enable the designer to record fluctuating pressures which are important at assessing the dynamic behaviour of buildings. It's clear that CFD can be used as an effective tool for structural design given that correct modelling techniques are adopted such as that presented in this paper.

Acknowledgement

The authors gratefully acknowledge the support of the Dr. Kapil Chauhan and the technical staff of the boundary layer wind tunnel at the University of Sydney. Authors would like to acknowledge the financial support they received from CERDS (Civil Engineering Research Development Scheme) from the school of Civil Engineering, University of Sydney.

References

1. Taranath, B.S., *Tall Building Design: Steel, Concrete and Composite Systems*. 2016, United States of America: CRC Press.
2. Holmes, J.D., *Wind loading of structures*. 2001: Taylor & Francis.
3. Scruton, C., *An introduction to wind effects on structures*. 1981, Oxford: Oxford University Press.
4. Standards Australia/New Zealand, *Structural design actions, Part 2: Wind actions, AS/NZS 1170.2:2011(R2016)*. 2011.
5. Irwin, P., *Wind engineering challenges of the new generation of super-tall buildings.* Journal of Wind Engineering and Industrial Aerodynamics, 2009. 97: p. 328-324.
6. Aly, A.M., *Pressure integration technique for predicting wind-induced response in high-rise buildings.* Alexandria Engineering Journal, 2013. 52(4): p. 717-731.
7. Roshko, A., *Experiments on the flow past a circular cylinder at very high Reynolds number.* Journal of Fluid Mechanics, 1961. 10(3): p. 345-356.
8. Achenbach, E., *Distribution of local pressure and skin friction around a circular cylinder in cross-flow up to Re = 5 × 10^6*. Journal of Fluid Mechanics, 1968. 34(04): p. 625-639.
9. Blocken, B., T. Stathopoulos, and J.P.A.J. van Beeck, *Pedestrian-level wind conditions around buildings: Review of wind-tunnel and CFD techniques and their accuracy for wind comfort assessment.* Building and Environment, 2016. 100: p. 50-81.

10. Elshaer, A., et al., *LES evaluation of wind-induced responses for an isolated and a surrounded tall building.* Engineering Structures, 2016. 115: p. 179-195.
11. Elshaer, A., G. Bitsuamlak, and A. El Damatty, *Enhancing wind performance of tall buildings using corner aerodynamic optimization.* Engineering Structures, 2017. 136: p. 133-148.
12. Huang, S., Q.S. Li, and S. Xu, *Numerical evaluation of wind effects on a tall steel building by CFD.* Journal of Constructional Steel Research, 2007. 63(5): p. 612-627.
13. Perén, J.I., et al., *CFD analysis of cross-ventilation of a generic isolated building with asymmetric opening positions: Impact of roof angle and opening location.* Building and Environment, 2015. 85: p. 263-276.
14. Franke, J., et al. *Recommendations on the use of CFD in wind engineering*. in *COST Action C14, Impact of Wind and Storm on City Life Built Environment*. 2004. von Karman Institute, Sint-Genesius-Rode, Belgium.
15. Anderson Jr, J., *Basic philosophy of CFD,* in *Computational Fluid Dynamics,* J.F. Wendt, Editor. 2009, Springer. p. 3-14.
16. ANSYS Inc., *ANSYS Fluent Theory Guide*. 2013, ANSYS, Inc. Southpointe 275 Technology Drive Canonsburg, PA.
17. Blazek, J., *Computational Fluid Dynamics: Principles and Applications*. 1 ed. 2001: Elsevier Science
18. Melbourne, W.H., *Comparison of measurements on the CAARC standard tall building model in simulated model wind flows.* Wind Engineering and Industrial Aerodynamics, 1980. 6(1-2): p. 73-88.
19. Braun, A.L. and A.M. Awruch, *Aerodynamic and aeroelastic analyses on the CAARC standard tall building model using numerical simulation.* Computers & Structures, 2009. 87(9-10): p. 564-581.
20. Dagnew, A.K. and G.T. Bitsuamlak, *Computational evaluation of wind loads on a standard tall building using LES.* Wind and Structures, 2014. 18(5): p. 567-598.
21. Zhang, Y., W.G. Habashi, and R.A. Khurram, *Predicting wind-induced vibrations of high-rise buildings using unsteady CFD and modal analysis.* Journal of Wind Engineering and Industrial Aerodynamics, 2015. 136: p. 165-179.
22. Meng, F.-Q., et al., *Sensitivity analysis of wind pressure coefficients on CAARC standard tall buildings in CFD simulations.* Journal of Building Engineering, 2018. 16: p. 146-158.
23. Obasaju, E.D., *Measurement of forces and base overturning moments on the CAARC tall building model in a simulated atmospheric boundary layer.* Journal of Wind Engineering and Industrial Aerodynamics, 1992. 40(2): p. 103-126.
24. Tominaga, Y., *Flow around a high-rise building using steady and unsteady RANS CFD: Effect of large-scale fluctuations on the velocity statistics.* Journal of Wind Engineering and Industrial Aerodynamics, 2015. 142: p. 93-103.
25. Liu, J. and J. Niu, *CFD simulation of the wind environment around an isolated high-rise building: An evaluation of SRANS, LES and DES.* Building and Environment, 2016. 96: p. 91-106.
26. Asghari Mooneghi, M. and R. Kargarmoakhar, *Aerodynamic Mitigation and Shape Optimization of Buildings: Review.* Journal of Building Engineering, 2016. 6: p. 225-235.
27. Bernardini, E., et al., *Aerodynamic shape optimization of civil structures: A CFD-enabled Kriging-based approach.* Journal of Wind Engineering and Industrial Aerodynamics, 2015. 144: p. 154-164.

28. Rahman, M.M., M.M. Karim, and M.A. Alim, *Numerical investigation of unsteady flow past a circular cylinder using 2-d finite volume method.* Journal of Naval Architecture and Marine Engineering, 2007. 4(1): p. 27-42.
29. Stringer, R.M., J. Zang, and A.J. Hillis, *Unsteady RANS computations of flow around a circular cylinder for a wide range of Reynolds numbers.* Ocean Engineering, 2014. 87: p. 1-9.
30. Xing, F., D. Mohotti, and K. Chauhan, *Experimental and numerical study on mean pressure distributions around an isolated gable roof building with and without openings.* Building and Environment, 2018. 132: p. 30-44.
31. ANSYS®, *Academic Research Fluent, Release 18*. 2017.
32. Miau, J.J., et al., *Experiment on smooth, circular cylinders in cross-flow in the critical Reynolds number regime.* Experiments in Fluids, 2011. 51(4): p. 949-967.
33. Deaves, D. and R. Harris, *A mathematical model of the structure of strong winds*, in *CIRIA Report 76*. 1978, Construction Industry Research and Information Association: London.
34. Standard Australian/New Zealand, *Structural design actions-Wind actions-Commentary (Supplement to AS/NZS 1170.2:2002)*. 2002.
35. Taranath, B.S., *Reinforced concrete design of tall buildings*. Vol. 2. 2010: CRC press London.
36. Blocken, B., *Computational Fluid Dynamics for urban physics: Importance, scales, possibilities, limitations and ten tips and tricks towards accurate and reliable simulations.* Building and Environment, 2015. 91: p. 219-245.
37. Tominaga, Y., et al., *AIJ guidelines for practical applications of CFD to pedestrian wind environment around buildings.* Journal of Wind Engineering and Industrial Aerodynamics, 2008. 96(10-11): p. 1749-1761.
38. Launder, B.E. and D.B. Spalding, *The Numerical Computation of Turbulent Flows.* Computer Methods in Applied Mechanics and Engineering, 1973. 3: p. 269-289.
39. Shih, T.H., et al., *A new k-ϵ eddy viscosity model for high reynolds number turbulent flows.* Computer and Fluids, 1995. 24(3): p. 227-338.
40. Wilcox, D.C., *Reassessment of the scale-determining equation for advanced turbulence models.* AIAA Journal, 1988. 26: p. 1299-1310.
41. Menter, F.R., *Two-equation eddy-viscosity turbulence model for engineering applications.* AIAA, 1994. 32(8): p. 1598-1605.
42. Menter, F.R., et al., *A Correlation-Based Transition Model Using Local Variables—Part I: Model Formulation.* Journal of Turbomachinery, 2006. 128(3): p. 413-422.
43. Langtry, R.B., et al., *A Correlation-Based Transition Model Using Local Variables—Part II: Test Cases and Industrial Applications.* Journal of Turbomachinery, 2006. 128(3): p. 423-434.
44. ANSYS Inc., *ANSYS Fluent User's Guide*. 2013, ANSYS, Inc. Southpointe 275 Technology Drive Canonsburg, PA.
45. Richards, P.J. and R.P. Hoxey, *Appropriate boundary conditions for computational wind engineering models using the k-ϵ turbulence model.* Journal of Wind Engineering and Industrial Aerodynamics, 1993. 46: p. 145-153.
46. Richards, P.J. and S.E. Norris, *Appropriate boundary conditions for computational wind engineering models revisited.* Journal of Wind Engineering and Industrial Aerodynamics, 2011. 99(4): p. 257-266.
47. Blocken, B., T. Stathopoulos, and J. Carmeliet, *CFD simulation of the atmospheric boundary layer: wall function problems.* Atmospheric Environment, 2007. 41(2): p. 238-252.

48. Elshaer, A., et al., *Variations in wind load on tall buildings due to urban development.* Sustainable Cities and Society, 2017. 34: p. 264-277.
49. Rodi, W., *Comparison of LES and RANS calculations of flow around bluff bodies.* Wind Engineering and Industrial Aerodynamics, 1997. 69-71: p. 55-75.
50. Murakami, S., *Comparison of various turbulence models applied to a bluff body.* Journal of Wind Engineering and Industrial Aerodynamics, 1993. 46 & 47: p. 21-36.
51. Tominaga, Y., et al., *Comparison of various revised k–e models and LES applied to flow around a high-rise building model with 1:1:2 shape placed within the surface boundary layer.* Journal of Wind Engineering and Industrial Aerodynamics, 2008. 96: p. 389-411.
52. Strelets, M., *Detached eddy simulation of massively separated flows.* AIAA Paper 2001-0879, 2001.
53. Menter, F.R., M. Kuntz, and R. Langtry, *Ten years of industrial experience with the SST turbulence model,* in *Turbulence, Heat and Mass Transfer 4*, K. Hanjalic, Y. Nagano, and M. Tummers, Editors. 2003: Begell House Inc.
54. Yan, B.W. and Q.S. Li, *Detached-eddy and large-eddy simulations of wind effects on a high-rise structure.* Computers & Fluids, 2017. 150: p. 74-83.
55. European Standards, *Eurocode 1: Actions on Structures - Part 1-4: General actions - Wind actions EN 1991-1-4*. 2005.